

## 32. Design, Fabrication and Control of Microactuators for Dual-Stage Servo Systems in Magnetic Disk Files

This chapter discusses the design and fabrication of electrostatic MEMS microactuators and the design of dual-stage servo systems in disk drives. It introduces fundamental requirements of disk drive servo systems, along with challenges posed as storage densities increase. It describes three potential dual-stage configurations and focuses on actuated slider assemblies using electrostatic MEMS microactuators. The authors discuss major electrostatic actuator design issues, such as linear versus rotary motion, electrostatic array configuration, and differential operation. Capacitive and piezoresistive elements may be used to sense relative slider position, while integrated gimbals and structural isolation may prove useful in improving performance. A detailed design example based on a translational, micromolded actuator illustrates several of these concepts and is accompanied by theoretical and experimental results.

The chapter continues to discuss MEMS microactuator fabrication. It describes several processes for obtaining appropriate electrostatic devices including micromolding, deep-reactive ion etching, and electroplating. The primary goal of these processes is to obtain very high-aspect ratio structures, which improve both actuation force and structural robustness. Other fabrication issues, such as electrical interconnect formation, material selection, and processing cost, are also considered. Actuated slider fabrication is compared to that of actuated suspension and actuated head assemblies; this includes instrumentation of a suspension with strain sensors to aid in vibration detection.

The section on controller design reviews dual-stage servo control design architectures and methodologies. The considerations for controller design of MEMS microactuator dual-stage servo systems are discussed. The details of control designs using a decoupled SISO design method and the robust multivariable design method of  $\mu$ -synthesis are also presented. In the decoupled design, a self-tuning control algorithm has been

32.1	<b>Design of the Electrostatic Microactuator</b>	952
32.1.1	Disk Drive Structural Requirements	952
32.1.2	Dual-Stage Servo Configurations	953
32.1.3	Electrostatic Microactuators: Comb-Drives vs. Parallel-Plates	954
32.1.4	Position Sensing	956
32.1.5	Electrostatic Microactuator Designs for Disk Drives	958
32.2	<b>Fabrication</b>	962
32.2.1	Basic Requirements	962
32.2.2	Electrostatic Microactuator Fabrication Example	962
32.2.3	Electrostatic Microactuator Example Two	963
32.2.4	Other Fabrication Processes	966
32.2.5	Suspension-Level Fabrication Processes	967
32.2.6	Actuated Head Fabrication	968
32.3	<b>Servo Control Design of MEMS Microactuator Dual-Stage Servo Systems</b>	968
32.3.1	Introduction to Disk Drive Servo Control	969
32.3.2	Overview of Dual-Stage Servo Control Design Methodologies	969
32.3.3	Track-Following Controller Design for a MEMS Microactuator Dual-Stage Servo System	972
32.3.4	Dual-Stage Seek Control Design	978
32.4	<b>Conclusions and Outlook</b>	979
	<b>References</b>	980

developed to compensate for the variations in the microactuator's resonance mode. In the  $\mu$ -synthesis design, robust controllers can be synthesized by using additive and parametric uncertainties to characterize the un-modeled dynamics of the VCM and the variations in the microactuator's resonance mode. The chapter also introduces a dual-stage short-span seek control scheme based on decoupled feed forward reference trajectories generations.

This chapter discusses the design and fabrication of electrostatic MEMS microactuators, and the design of dual-stage servo systems, in disk drives. The focus of the chapter is an actuated slider assembly using an electrostatic MEMS microactuator. We discuss major design issues, including linear versus rotary actuation, electrostatic array configuration, and integrated sensing capability. We describe several fabrication processes for obtaining the necessary devices, such as micromolding, deep-reactive ion etching, and electroplating. Dual-stage servo control design architectures and methodologies are reviewed as well. We also present in detail track-following controller designs based on a sensitivity function decoupling single-input-single-output design methodology and the robust  $\mu$ -synthesis design methodology. Finally we introduce a 2-DOF short span seek control design using dual-stage actuator.

Since the first hard disk drive (HDD) was invented in the 1950s by IBM, disk drives' storage density has been following Moore's law, doubling roughly every 18 months. The current storage density is 10 million times larger than that of the first HDD [32.1]. Historically, increases in storage density have been achieved by almost equal increases in track density, the number of tracks encircling the disk, and bit density, the number of bits in each track. But, because of superparamagnetism limitations, future areal storage density increases in HDDs are predicted to be achieved mainly through an increase in track density [32.2].

Research in the HDD industry is now targeting an areal density of one terabit per square inch. For a predicted bit aspect ratio of 4 : 1, this translates to a linear bit density of 2 M bits per inch (BPI) and a radial track density of 500 K tracks per inch (TPI), which in turn implies a track width of 50 nm. A simple rule of thumb for servo design in HDDs is that three times the statistical standard deviation of the position error between the head and the center of the data track should be less than 1/10 of the track width. Thus, to achieve such a storage

density, nanometer-level precision of the servo system will be required.

A disk drive stores data as magnetic patterns, forming bits, on one or more disks. The polarity of each bit is detected (read) or set (written) by an electromagnetic device known as the read/write head. The job of a disk drive's servo system is to position the read/write head over the bits to be read or written as they spin by on the disk. In a conventional disk drive, this is done by sweeping over the disk a long arm consisting of a voice coil motor (VCM), an E-block, suspensions, and sliders, as shown in Figs. 32.1 and 32.2. A read/write head is fabricated on the edge of each slider (one for each disk surface). Each slider is supported by a suspension and flies over the surface of disk on an air-bearing. The VCM actuates the suspensions and sliders about a pivot in the center of the E-block. We describe this operation in more detail in the following section.

The key to increasing HDD servo precision is to increase servo control bandwidth. But, the bandwidth of a traditional single-stage servo system as shown in Fig. 32.2 is limited by the multiple mechanical resonance modes of the pivot, the E-block, and the suspension between the VCM and the head. Nonlinear friction of the pivot bearing also limits achievable servo precision. Dual-stage actuation, with a second stage actuator placed between the VCM and the head, has been proposed as a solution that would increase servo bandwidth and precision.

Several different secondary actuation forces and configurations have been proposed, each having strengths and weaknesses given the requirements of HDDs. The dual-stage configurations can be categorized into three groups: actuated suspension, actuated slider, and actuated head. Within these, actuation forces include piezoelectric, electrostatic, and electromagnetic. In this chapter, we discuss design, fabrication and control of an electrostatic MEMS microactuator (MA) for actuated slider dual-stage positioning.

## 32.1 Design of the Electrostatic Microactuator

The servo system of a hard disk drive is the mechatronic device that locates and reads data on the disk. In essence, it is a large arm that sweeps across the surface of the disk. At the end of the arm is the read-write head, containing the magnetic reading and writing elements that transfer information to and from the disk.

### 32.1.1 Disk Drive Structural Requirements

This read-write head is contained in a box-like structure known as a slider. The slider has a contoured lower surface that acts as an air bearing between the head and the disk. The high-velocity airflow generated by

the spinning disk pushes up on the air-bearing surface, maintaining the slider and read-write head at a constant distance from the disk, despite unevenness of the disk, permitting reliable data reading and writing.

The arm over an HDD's disk has three primary stages: the voice-coil motor (VCM), the E-block, and the suspension. In a conventional disk drive, the VCM performs all positioning of the head, swinging it back and forth across the disk. The E-block lies between the VCM and the suspension and contains the pivot point. The suspension projects from the E-block over the disk as a thin flexible structure, generally narrowing to a point at the location of the slider.

For a disk drive servo to operate effectively, it must maintain the read-write head at a precise height above the disk surface and within a narrow range between the disk tracks arranged in concentric circles around the disk. It must also be able to seek from one track to another. Information about the track that the head is following is encoded in sectors radiating from center of the disk, allowing the head to identify its position and distance from the center of the track. To maintain a correct flying height, the suspension must be designed with an appropriate stiffness in the vertical direction to balance an air-bearing force corresponding to the slider design in use in the drive. Meanwhile, the suspension must be flexible to roll and pitch at the slider location to permit adaptation to unevenness of the disk surface. This is accomplished using a gimbal structure. The suspension as a whole, however, should not bend or twist during the operation, as this would misdirect the head away from the track it is following.

As data densities in HDDs increase and track widths diminish, single-stage, conventional servo systems become less able to position the head precisely. Because the VCM/E-block/suspension assembly is large and massive as a unit, the speed at which the head can be controlled is limited. Furthermore, the assembly tends to have a low natural frequency, which can accentuate vibration in the disk drive and cause off-track errors. At track densities approaching one Terabit per square inch in the future, the vibration induced by airflow in a disk drive alone is enough to force the head off-track.

A solution to these problems is to complement the VCM with a smaller, secondary actuator to form a dual-stage servo system. The VCM continues to provide rough positioning, while the second stage actuator does fine positioning and damps out vibration and other disturbances. The smaller second stage actuator can typically be designed to have a much higher natural frequency and less susceptibility to vibration than the

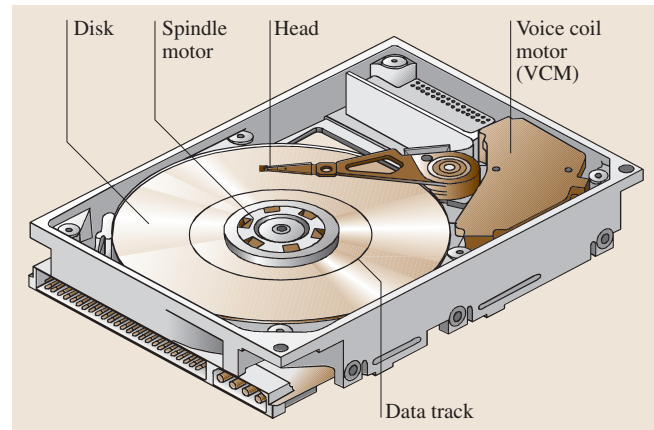


**Fig. 32.1** A schematic diagram of an HDD

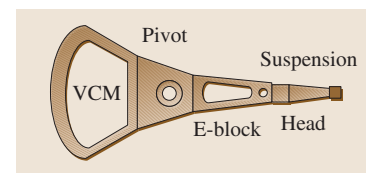


**Fig. 32.2** VCM actuator in an HDD

VCM. Any actuator used in a dual-stage system should be inexpensive to build, require little power to operate, and preserve the stiffness properties described above necessary to preserve the flying height.

### 32.1.2 Dual-Stage Servo Configurations

In the past six years, much research work has been dedicated to the exploration of suitable secondary actuators for constructing dual-stage servo systems for HDDs. These dual-stage configurations can be categorized into three groups: “actuated suspension,” “actuated slider,” and “actuated head.”

#### Actuated Suspension

In this approach, the suspension is redesigned to accommodate an active component, typically a piezoelectric material. This piezoelectric material stretches or flexes the suspension to position the slider and magnetic head. Piezoelectric material is an active actuation element that produces a large actuation force but small actuation stroke. In the “actuated-suspension” configuration, therefore, the piezoelectric actuators are usually implemented in a leverage mechanism that can convert small actuation displacements into large head displacements. Typically this is done by placing the piezoelectric

actuators away from the magnetic head (between the E-block and suspension) so that they can have a long leverage arm to gain mechanical amplification and produce a sufficient magnetic-head motion. The advantage of this approach is that the suspension can be fabricated by a conventional suspension-making process, and its dual-stage servo configuration is effective in attaining low frequency runout attenuation in the positioning servo loop. The major drawback of this approach is that the system is still susceptible to instabilities due to the excitation of suspension resonance modes. Thus, track-per-inch (TPI) servo performance can be increased but remains limited when compared to the next two approaches. This approach, however, is expected to be the first deployed in commercial HDDs [32.3, 4].

#### Actuated Slider

In this approach, a microactuator is placed between the slider and gimbal to position the slider/magnetic heads. The resulting servo bandwidth can be higher than the previous approach because the secondary actuation bypasses the mechanical resonances of the suspension. This approach uses existing sliders and microactuators that can be batch fabricated, and thus could be cost effective. But, the size and mass of the microactuator are significant relative to those of current sliders and may interfere with the slider flying stability. Current suspensions, therefore, need to be redesigned to adopt this secondary actuator. Suitable driving forces in this approach include electrostatic, electromagnetic, and piezoelectric [32.5–8]. To further reduce the assembly task of placing the microactuator in between gimbal structure and slider, some researchers have proposed microactuators that are either integrated with the gimbal structure [32.6] or the slider [32.9].

#### Actuated Head

In this approach, the slider is redesigned so that the microactuators can be placed inside the slider block and actuate the magnetic heads with respect to the rest of the slider body. As these microactuators are very small, they only slightly increase the slider weight and are thus capable of working with the current suspension assembly. Researchers have successfully demonstrated the integrated fabrication process for fabricating the electrostatic microactuators and magnetic heads within one piece of ceramic block (slider). The embedded electrostatic microactuator has its resonance close to 30 kHz and was able to position the magnetic heads relative to the rest of the slider body by  $0.5\ \mu\text{m}$  [32.10, 11]. Full-

fledged integration of slider, actuator, and read/write head remains a challenge.

In this chapter, we focus on actuated slider configurations, as they involve a great deal of interesting microscale engineering. In particular, we will discuss electrostatic actuation, probably the most common method of implementing microactuation in microelectromechanical devices. Any such microactuator will exhibit certain features:

- a fixed base, which attaches to the suspension,
- a movable platform, upon which the slider rests,
- springs between the base and platform, flexible in the direction of desired motion, and stiff in all other directions, and
- an electrostatic actuation array that generates the force used to move the platform and slider.

Microactuators must also include a wiring scheme for transferring signals to and from the slider and often incorporate a structure for sensing the motion of the slider relative to the suspension. Electrostatic microactuators to be discussed in this chapter include HexSil and DRIE fabricated actuators from the University of California, Berkeley, and electroplating-formed actuators by IBM and the University of Tokyo.

Electromagnetic or piezoelectric force are alternatives to electrostatic actuation in the actuated-slider configuration. Electromagnetic microactuators use ferromagnetic films to produce force perpendicular to an applied electric field. This type of actuation has potentially low voltage requirements but requires special fabrication techniques to integrate the magnetic components into the assembly. A microactuator of this type for hard disk drives is under development at Seagate, with results as yet unpublished. Piezoelectric microactuators use a piezoelectric material, which expands or contracts in response to applied voltage, to move the slider. These actuators have simple fabrication, the patterning a piece of piezoelectric material to sit between the suspension and slider, but it is difficult to obtain an adequate range of motion. A short stroke from the piezoelectric piece must be leveraged into a much larger motion at the read/write head. A piezoelectric microactuator has been produced by TDK corporation with a  $0.5\ \mu\text{m}$  stroke length at 10 V, with a 10 V bias [32.12].

### 32.1.3 Electrostatic Microactuators: Comb-Drives vs. Parallel-Plates

Electrostatic microactuators have been studied as the secondary actuators in HDDs for their relative ease

<sup>1</sup>TS “um” has been changed to “μm”. Please confirm.

of fabrication, particularly in the configurations of “actuated slider” and “actuated head,” since the structural material needs only to be conductive rather than ferromagnetic or piezoelectric. Electrostatic force is generated by applying a voltage difference between the moving shuttle and a fixed stator element. Depending on the designated motion for the shuttle, electrostatic actuators are often categorized into two groups: comb-drives and parallel-plates, as illustrated in Fig. 32.3.

The magnitude of the electrostatic force generated equals the rate of change of energy that is retained within the finger-like structure and varied by shuttle motion. Therefore, the electrostatic force for comb-drive actuators, in which the designated shuttle motion moves along the  $x$ -direction, as shown in Fig. 32.3, equals

$$F_{\text{comb}} = \frac{\partial E}{\partial x} = \frac{\epsilon h}{2d} V^2, \quad (32.1)$$

where  $\epsilon$  is the permittivity of air,  $x$  is the overlap between two adjacent plates,  $h$  is plate thickness, and  $d$  is the gap between two parallel plates. Similarly, the electrostatic force for parallel-plates actuators is

$$F_{\text{parallel}} = \frac{\partial E}{\partial y} = \frac{\epsilon x h}{2d^2} V^2. \quad (32.2)$$

As indicated in (32.1) and (32.2), the electrostatic force for comb-drives actuators does not depend on the displacement of the moving shuttle and thus allows a long stroke while maintaining a constant electrostatic force. The electrostatic force for parallel-plates actuators, in contrast, is a nonlinear function of its shuttle motion ( $\propto 1/d^2$ ), and the maximum stroke is limited by the nominal gap between shuttle and stator. A longer stroke is achieved with a larger gap, at the expense of lower electrostatic force. For applications that require small stroke but large force output, parallel-plates actuators are preferred since the output force from parallel-plates can be  $x/d$  times larger than the force from comb-drives. The following equation (32.3) is easily derived from (32.1) and (32.2).

$$\frac{F_{\text{parallel}}}{F_{\text{comb}}} = \frac{x}{d}. \quad (32.3)$$

A simplified second-order differential equation is often utilized to describe the dynamic response of an electrostatic microactuator

$$m\ddot{x}(t) + b\dot{x}(t) + K_m x(t) = F[V, x(t)], \quad (32.4)$$

where  $m$  is the mass of the moving shuttle,  $b$  is the damping coefficient of the microactuator,  $K_m$  is the spring

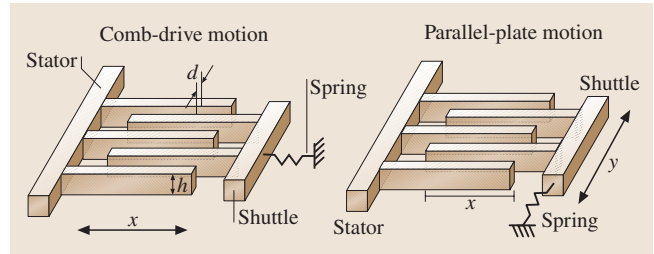


Fig. 32.3 Electrostatic microactuators. Comb-drives versus parallel-plates

constant of the mechanical spring that connects the moving shuttle to an anchor point, and  $F$  is the electrostatic force that can be obtained from (32.1) and (32.2).

### Differential Drives

Because electrostatic force is always attractive, electrostatic microactuators need other features to actively control the direction of shuttle motion in servo applications, as opposed to relying on the restoring force from a mechanical spring. For this reason, the differential-drives approach, as shown in Fig. 32.4, is frequently adopted in electrostatic microactuator designs. Based on the differential-drive configuration, the simplified second-order differential equation (32.4) is rewritten as,

$$m\ddot{x}(t) + b\dot{x}(t) + K_m x(t) = F[V_{\text{bias}} + V_{\text{dr}}, x_o - x(t)] - F[V_{\text{bias}} - V_{\text{dr}}, x_o + x(t)], \quad (32.5)$$

where  $x_0$  is the nominal position of the moving shuttle. If the differential drive is operated at the bias voltage ( $V_{\text{bias}}$ ) with a small perturbation voltage ( $V_{\text{dr}}$ ), the nonlinear force input in (32.5) can be linearized with a first-order

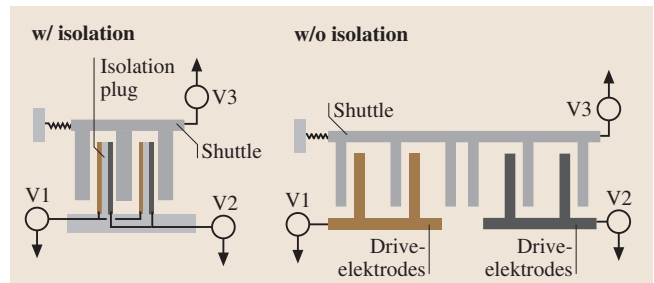


Fig. 32.4 Differential parallel-plates actuators and electrical-isolation features

approximation.

$$\begin{aligned} m\ddot{x}(t) + b\dot{x}(t) + (K_m - K_e)x(t) &= K_v V_{dr} \\ K_e &= 2 \frac{\partial F}{\partial x} \Big|_{V_{bias}} \\ K_v &= 2 \frac{\partial F}{\partial V_{dr}} \Big|_{V_{bias}} \end{aligned} \quad (32.6)$$

Here  $K_e$  represents a softening electrostatic spring constant, and  $K_v$  represents the voltage-to-force gain. The electrostatic spring constant acts as a negative spring during the electrostatic microactuator operation, and its value varies with the bias voltage ( $V_{bias}$ ). When the electrostatic spring constant  $K_e$  exceeds the spring constant  $K_m$  from the mechanical spring, the microactuator becomes unstable; this is often described as pull-in instability. As shown in (32.5) and (32.6), the differential configuration cancels the even order harmonics in voltage and thus linearizes the voltage–force relation to some extent. Furthermore, in parallel-plates actuators, the differential configuration reduces the nonlinearity in actuation voltage as well as in shuttle displacement.

### Electrical Isolation

Because electrostatic actuation requires multiple voltage levels for actuation force and position sensing (as discussed in the following section), electrical isolation is another challenge for designing an electrostatic microactuator. Generally speaking, when multiple voltage levels are needed in MEMS devices, electrical isolation is achieved by breaking up the parts that need to be on different voltage level and anchoring them separately to a nonconductive substrate. This approach has many drawbacks, not only because it requires a substrate in a device but also because structures have to be mechanically separated to be electrically isolated. The electrical isolation problem is far more severe in parallel-plates microactuators than comb-drive microactuators since parallel-plates actuation generally requires different voltage levels for stator fingers pulling in opposite directions.

Figure 32.4 shows an example of how an electrical-isolation feature can be utilized to increase the actuation force output in a differential parallel-plates microactuator design. As shown in the figure, without the proper electrical isolation, drive-electrodes with different voltage potentials have to be placed in separate groups and result in the same voltage difference across drive-electrodes and shuttle on both sides of each shuttle finger [32.5, 6]. Since electrostatic forces are always attractive, gaps on two sides of the interlaced structure cannot be made equal, otherwise the forces on two

sides of a shuttle finger will be equal and the shuttle’s movement direction will be uncontrollable. With such electrical-isolation features as the “isolation plug,” shown on the left in Fig. 32.4, gaps of the interlaced structure can be the same width, since different voltages can be applied on the two sides of the shuttle fingers. As shown in Fig. 32.4, the design with integrated electrical-isolation features is more compact than without isolation features. Consequently, more finger structures can fit in the same amount of space, and the actuation voltage can be reduced.

### 32.1.4 Position Sensing

Most proposed HDD dual-stage servo controllers utilize only the position of the magnetic head relative to the center of data track, known in the industry as the position error signal, or PES, for closed-loop track following control. These systems have a single-input-multi-output (SIMO) control architecture. In some instances, however, it is also possible to measure the relative position error signal (RPES) of the magnetic head relative to the VCM. In this case, the control architecture is multi-input-multi-output (MIMO). As shown in [32.13], RPES can be used in a MIMO controller to damp out the second stage actuator’s resonance mode and enhance the overall robustness of the servo system.

Capacitive position sensing and piezoresistive position sensing are two popular sensing mechanisms among electrostatic microactuator designs. Each of these sensing mechanisms is discussed in more detail in the following sections.

#### Capacitive Position Sensing

Capacitive position sensing is based on shuttle movement causing a capacitance change between the moving shuttle and fixed stators. By measuring the change in capacitance, it is possible to determine the shuttle location relative to the fixed stator. The output voltage ( $V_o$ ) for both differential drives in Fig. 32.5 equals  $2\delta C/C_i V_s$ . The capacitance change due to shuttle movement ( $dC/dx$ ) can be derived and the output voltage ( $V_o$ ) for the comb-drives and parallel-plates can be formulated as a function of shuttle displacement.

$$\begin{aligned} V_{comb} &= 2 \frac{C_s}{C_i} \frac{\delta x}{x_0} V_s, \\ V_{parallel} &= 2 \frac{C_s}{C_i} \frac{y_0 \delta y}{y_0^2 - \delta y^2} V_s, \\ &\approx 2 \frac{C_s}{C_i} \frac{\delta y}{y_0} V_s, \end{aligned} \quad (32.7)$$

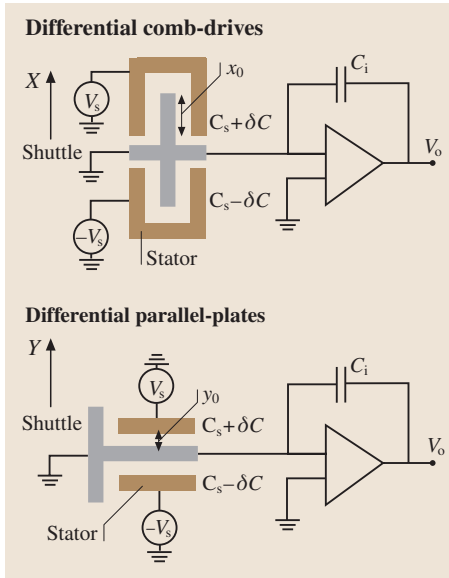


**Fig. 32.5** Capacitive position sensing. Comb-drives versus parallel-plates motion

where  $x_0$  is the nominal overlap for interlaced fingers and  $y_0$  is the nominal gap between overlapped fingers, as shown in Fig. 32.5.

As indicated by (32.7), the voltage output for comb-drives sensing structure,  $V_{comb}$ , is linear with shuttle displacement. On the other hand, the sensing configuration that makes use of parallel-plates motion has better sensitivity for detecting shuttle motion since  $y_0$  is usually smaller than  $x_0$ . Although the nonlinearity in parallel-plates sensing can be linearized by the differential drive configuration to some extent, in a design example of  $4\ \mu\text{m}$  gap with  $1\ \mu\text{m}$  stroke, the linear model shown in (32.7) still produces 6% deviation from the nonlinear model.

Among electrostatic microactuators that use capacitive position sensing, the capacitance variation due to shuttle motion ( $dC/dx$ ) is typically at the level of  $100\ \text{fF}/\mu\text{m}$ . In order to obtain 10 nm position sensing resolution, the capacitance sensing circuit must be able to detect capacitance variation of 1 fF in the presence of parasitic capacitance and offset/mismatches from op-amps, which can easily result in an output voltage orders of magnitude larger than the output voltage from the designated capacitance variation. In most capacitive position sensing, the limiting factor for the sensing resolution is not the thermal noise but the sensing circuit's design.

Here we introduce two basic capacitance sensing circuits suitable for high-resolution position sensing [32.14]. The concept of the “synchronous scheme,” as shown in Fig. 32.6, is to reduce the impedance of sense capacitors as well as the offset and  $1/f$  noises from op-amps by applying modulation techniques on the sense voltage ( $V_s$ ). The  $R_{dc}$  resistor on the feedback loop sets the DC voltage level at the input nodes of the “charge integrator.” The effect of the presence of parasitic capacitance ( $C_p$ ) is nullified by the virtual ground condition from the op-amps. The major drawback of the synchronous scheme is that the DC-setting resistor ( $R_{dc}$ ) has to be large to ensure the proper gain for the capacitance sensing [32.14], which introduces excessive thermal noise into the sensing circuit. In addition, a large resistor usually consumes a large die space in implementation.

A switched-capacitance scheme, as shown at the bottom in Fig. 32.6, is one alternative that avoids the use of DC-setting resistor. The capacitance sensing period is broken into two phases: reset phase and sense phase. During the reset phase, input/output nodes of capacitors

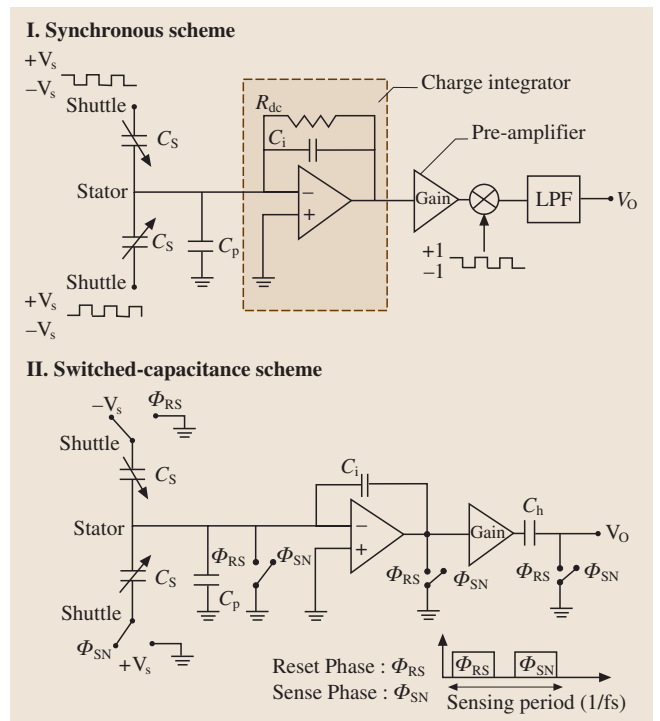


**Fig. 32.6** Capacitive position sensing circuits. Synchronous scheme versus switched-capacitance scheme

and input voltage to op-amps are set to ground or reference level to ensure proper DC voltage for the charge integrator. During the sense phase, sense voltage  $\pm V_s$  is applied to the sense capacitors, and the amount of charge proportional to the mismatch in the sense capacitors is integrated on the capacitor  $C_i$ , thus producing an output voltage proportional to the capacitance mismatch from the sense capacitors. This approach replaces the large DC-setting resistor by capacitors and switches and results in a much smaller die compared to the synchronous scheme. Furthermore, the switching technique allows more design flexibility for system integration and performance improvement because of the ability to allocate separate phases for various operations. The major drawback of this design is that it draws noise into sensing circuits from switches and sampling capacitor  $C_h$ . But, these noises can be compensated by dividing the sense phase into 2 ~ 3 sub-sense phases [32.14], at the expense of a complicated circuit design.

### Piezoresistive Sensing

Piezoresistive films have been widely used as strain-sensitive components in a variety of MEMS devices, including pressure sensors and vibration sensors. Generally speaking, piezoresistive sensing techniques require less complicated sensing circuits and perform better in a severe environment than other sensing techniques. When a piezoresistive film is subjected to stress, the film resistivity and dimensions change. The fractional change of resistance is proportional to the deformation of the piezoresistive film. For a small change of resistance, this relation can be expressed as,

$$\frac{\Delta R}{R} = K \cdot \epsilon, \quad (32.8)$$

where  $R$  is resistance of the piezoresistive film,  $K$  is its gage factor and  $\epsilon$  is strain. In microactuator designs, the piezoresistive film is usually applied to the spring structure that connects the moving shuttle to an anchor point. When the shuttle moves, it stretches the spring as well as the piezoresistive film, consequently, the piezoresistive film produces a deformation signal proportional to the shuttle displacements. As a result, piezoresistive sensing is easier to implement than capacitive position sensing, but the sensing resolution is usually less accurate due to higher thermal noises introduced by the resistance of the piezoresistive film.

Another application of piezoresistive sensing, aside from measuring relative slider position, is to detect vibration in the suspension itself. The idea is to sense airflow-induced vibration of the suspension and feed that

information forward to an actuated slider to damp out motion at the head. Piezoresistors used for this purpose can be made from metal or semiconductor materials, arranged as a strip or series of strips oriented along the direction of vibration strain. It is important that these sensors observe all vibration modes that contribute to off-track error, so a number of optimization schemes for locating the sensors have been developed [32.15]. One method is to maximize the minimum eigenvalue of the observability matrix of the sensor or sensors. This ensures that all relevant modes are observed. Another method is to minimize a linear quadratic gaussian control problem over potential sensor locations [32.16]. This serves to determine an optimal placement from the perspective of a linear controller.

### 32.1.5 Electrostatic Microactuator Designs for Disk Drives

Various electrostatic microactuators have been designed for the secondary actuation in HDDs. To incorporate an electrostatic microactuator into a HDD without altering much of current suspension configuration, many design constraints are imposed. In this section, we will first discuss some design issues and then present one specific design example.

#### Translational Microactuators versus Rotary Microactuators

Depending on the motion of the magnetic head actuated, microactuator designs are categorized into two groups: translational actuators and rotary actuators. Either type can be implemented by comb-drives [32.8, 17] or parallel-plates [32.5, 6, 18] actuation.

When employing a translational microactuator in a dual-stage HDD servo, previous research [32.13] has shown that a force coupling between the suspension and the translational microactuator exists, consisting of transmitted actuation force from the VCM and suspension vibration induced by windage. The force coupling from the VCM not only complicates the dual-stage servo controller but also imposes a design constraint on a translational microactuator design, in that the translational microactuator has to provide a large force output to counterbalance the coupling force. When the VCM makes a large movement, as in seeking a new data track, the microactuator may be overpowered. One solution is to pull the actuator to one side and lock it momentarily in place. Even then, the use of the two actuation-stages must be carefully coordinated to moderate the influence of the VCM on the microactuator. On the other

hand, the linear springs in the translational microactuator can also aid in damping out motion of the suspension. The portion of suspension vibration induced by windage mostly consists of high frequency excitation, so the resulting magnetic head's position error can be passively attenuated by low resonant frequency translational microactuators.

Generally speaking, rotary actuators are more difficult to design/analyze than translational actuators because of their nonuniform gap between shuttle and stator. Still, their different operating properties have both strengths and weaknesses. Unlike a translational actuator, no obvious force coupling is transmitted from the suspension to a rotary actuator, as the microactuator is nearly always attached to the end of suspension at the microactuator's center of rotation, which acts as a pivot point. With no mechanical coupling, the dual-stage servo system using a rotary microactuator does not suffer from the force coupling between VCM and microactuator seen in translational designs. But, the rotary microactuator has to compensate for the magnetic head's position error induced by suspension vibration without any passive attenuation of the vibration. Overall, a rotary actuator is likely to behave better than a translational microactuator during track seeking and worse during track following.

### Gimballed Microactuator Design

Proper flying height and orientation of a slider and read-write head over a hard disk is maintained by the interaction of the suspension, the air bearing of the slider, and a gimbal structure. The gimbal structure is located at the tip of the suspension and holds the slider/microactuator in its center coupon. The dynamic characteristic requirements of gimbal structures are that they be flexible in pitch and roll motion but stiff in in-plane and out-of-plane bending motion. To meet all these requirements using only one piece of metal is a highly challenging task. For this reason, most commercially available suspension/gimbal designs consist of two to three pieces of steel, each with different thickness.

The goal of a gimballed microactuator design is to integrate seamlessly an actuator and gimbal into a one-piece structure, as shown in Fig. 32.7, to simplify both suspension design and HDD assembly. A full integrated suspension that includes suspension, gimbal, and microactuators in one part has also been proposed [32.19]. The dimple structure, existing in most current gimbal structures, is excluded from the gimballed microactuator design and electrical interconnects

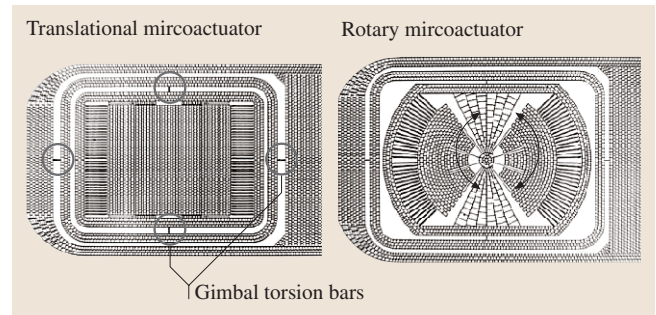


**Fig. 32.7** Schematics of translational microactuator versus rotary microactuator. Courtesy from Lilac Muller

are in situ fabricated on the gimballed microactuator, replacing the flexible cable in current HDD suspension assembly.

The dimple structure in current suspension assemblies provides out-of-plane stiffness while preserving the necessary torsional compliance in the gimbal structure. Without a dimple structure in the suspension assembly, the gimbal itself must provide high out-of-plane bending stiffness. Otherwise it would unbalance the suspension pre-load, which is an overbend of the suspension that balances the upward air-bearing force on the suspension during operation. The electrical interconnects are implemented to transmit data between magnetic heads, located at the center coupon of the gimbal structure, and IC circuits located at the end of the suspension. The in situ fabricated electrical interconnects are inevitably passed through torsion bars of the gimbal and thus set a design constraint for the minimum width of torsional bars. Furthermore, both the gimbal structure and microactuator should be the same thickness to simplify the MEMS fabrication process.

To summarize the design constraints discussed above, the integrated gimbal structure has to meet performance requirements with a single, uniform piece of material that would previously have been achieved by two to three metal pieces with different thicknesses, while the minimum width of any torsion bars that may be used pre-determined. To solve this problem, Muller [32.6] proposed a T-shaped structure (a beam structure with overhang surface sheet) for the torsion bars, and Chen [32.19] proposed “double-flexured” torsion bars. Additionally, many suspension manufacturers have developed new gimbal structures for their suspensions designed specifically for use with MEMS microactuators, moving the gimbal location back to the suspension from the microactuator.

### An Electrostatic Microactuator Design Example

Figure 32.8 shows a translational microactuator design suitable for the HDD dual-stage actuation by *Horsley* in 1998 [32.5]. The translational electrostatic microactuator dimensions are  $2.2 \text{ mm} \times 2.0 \text{ mm} \times 0.045 \text{ mm}$  and weight  $67 \mu\text{g}$ . The dimensions of the pico-slider on the top are  $1.2 \text{ mm} \times 1.0 \text{ mm} \times 0.3 \text{ mm}$  and weight  $1.6 \text{ mg}$ . This microactuator design does not include “electrical-isolation” features, and thus the electrical isolation and electrical-interconnects were fabricated on a separate substrate and subsequently bonded to the microactuator. This microactuator uses parallel-plates for actuation force but does not have dedicated position

sensing structures due to fabrication process limitation. Table 32.1 summarizes key parameters of this microactuator design.

Based on these parameters, the characteristics of this electrostatic microactuator can be estimated by the linear differential equation shown in (32.6).

Figure 32.9 shows the schematics of a circuit design by *Wongkomet* in 1998 [32.14], in which actuation driving voltage and capacitive position sensing were implemented for the electrostatic microactuator designed by *Horsley*. As mentioned before, the electrostatic microactuator design doesn't have dedicated structure for a position sensing; as a consequence, the input nodes for actuation and output nodes for capacitive position sensing have to share the same electrodes. Capacitors  $C_c$  and  $C_{c0}$ , shown in Fig. 32.9, are carefully designed to shield the high voltage presented in actuation circuit from sensing circuit, which is mostly low voltage, and thus enable driving/sensing circuit integration.

The driving circuit, shown in the left in Fig. 32.9, demonstrates how to generate the bias voltage ( $V_{\text{bias}}$ ,  $\pm 40 \text{ V}$ ) and drive voltage ( $V_{\text{dr}}$ ,  $-40$ – $+40 \text{ V}$ ) from the 0–5 V CMOS compatible circuits. The switches at the output of charge pumps were synchronized with the switching period  $\phi_{\text{RS}}$ . During the sense phases  $\phi_{\text{SN1}}$  and  $\phi_{\text{SN2}}$ , therefore, the switches are left open and thus no voltage fluctuation is seen by the sensing circuits. This

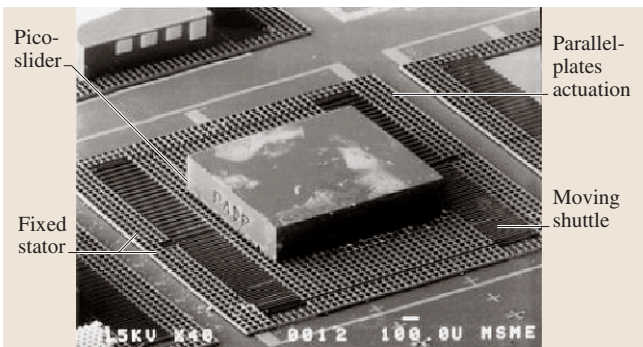


**Fig. 32.8** Pico-slider mounted on a translational microactuator. Courtesy from *Horsley* 1998

**Table 32.1** Parameters of the electrostatic microactuator design by *Horsley* 1998 [32.5]

Parameters	Source*	Value
Nominal gap	D	$10 \mu\text{m}$
Structure thickness	D	$45 \mu\text{m}$
Rotor mass, $m$	I	$44 \mu\text{g}$
$dC/dx$	C	$68 \text{ fF}/\mu\text{m}$
Actuation voltage, bias voltage	D	$40 \text{ V}$
Actuation voltage, maximum driving voltage	D	$\pm 40 \text{ V}$
Voltage-to-force gain $K_v$	I	$50 \text{ nN}/\text{V}$
Mechanical spring constant $K_m$	I	$29 \text{ N}/\text{m}$
Electrostatic spring constant $K_e$	I	$9.6 \text{ N}/\text{m}$
Damping coefficient, $b$	I	$1.03 \times 10^{-4} \text{ N}/(\text{m}/\text{s})$
Voltage-to-position DC gain	M	$0.05 \mu\text{m}/\text{V}$
Resonance frequency, $w_r$	M	$550 \text{ Hz}$

\*: D=Design value, C=Calculation, M=Measurement, I=Inferred from measurements

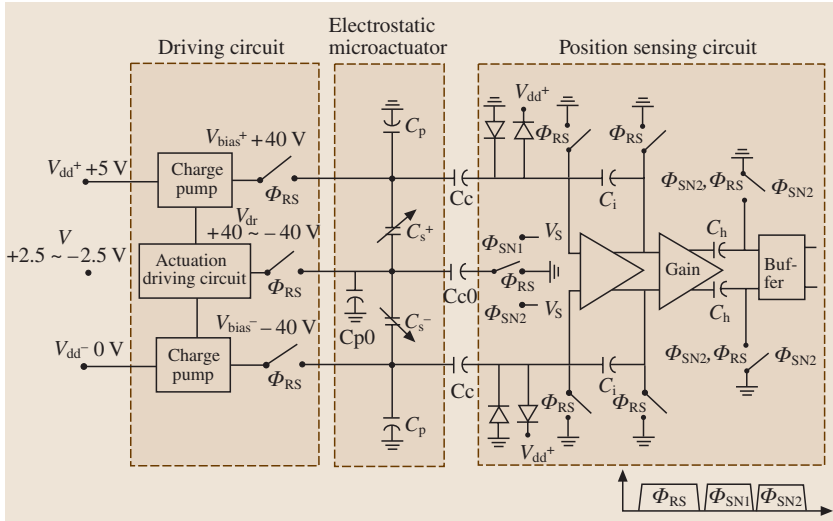


**Fig. 32.9** A simplified schematic including driving and sensing circuits for the electrostatic microactuator. Courtesy from Wongkomet 1998

arrangement was utilized to reduce feedthrough from the driving circuit to position sensing circuit.

The design target for the capacitive position sensing circuit was to achieve position sensing resolution of 10 nm, and this goal was approached by two main techniques implemented in the circuit: differential sensing and Correlated-Double-Sampling (CDS). The main benefits of the differential sensing scheme are reduced noise coupling and feedthrough, elimination of even-order harmonics, and improvement of dynamic range by doubling the output swing. To adapt this differential sensing scheme in a differential parallel-plates electrostatic microactuator, a bias voltage ( $V_{bias}$ ) was applied to the stator and the drive voltage ( $V_{dr}$ ) was applied to the shuttle. The CDS technique, a modified capacitance sensing technique based on the switched-capacitance scheme, was implemented along with the differential sensing scheme to compensate for sensing noises including  $1/f$ ,  $KT/C$ , switch charge injection and offset from op-amps [32.14]. The concepts of CDS can be briefly described as follows: the sense period is broken into three phases: one reset phase,  $\phi_{RS}$ , and two sense phases,  $\phi_{SN1}$  and  $\phi_{SN2}$ . During the  $\phi_{RS}$  sense phase, the voltages for capacitors and input nodes to op-amps are set to the reference level of the DC-voltage setting for the charge integrator, same as for the switched-capacitance scheme discussed in Sect. 32.1.4. During the  $\phi_{SN1}$  sense phase, a sensing voltage  $-V_s$  is applied to the shuttle and results in a voltage difference,  $\alpha(-V_s) + V_{error}$ , across the sampling capacitor  $C_h$ , where  $\alpha$  is the transfer function from

sense voltage to the output voltage at the pre-amplifier, shown as  $Gain$  in the plot, and  $V_{error}$  is the voltage at the output node of pre-amplifier resulting from noise, leakage charge, and offset of op-amps. Lastly, during the  $\phi_{SN2}$  sense phase, the sensing voltage is switched from  $-V_s$  to  $V_s$  and the switch next to  $C_h$  is switched open. This results in a voltage output  $\alpha(V_s) + V_{error}$  at the output node of the pre-amplifier and a voltage,  $2\alpha(V_s)$ , at the input node of the buffer. As a consequence, the volt-

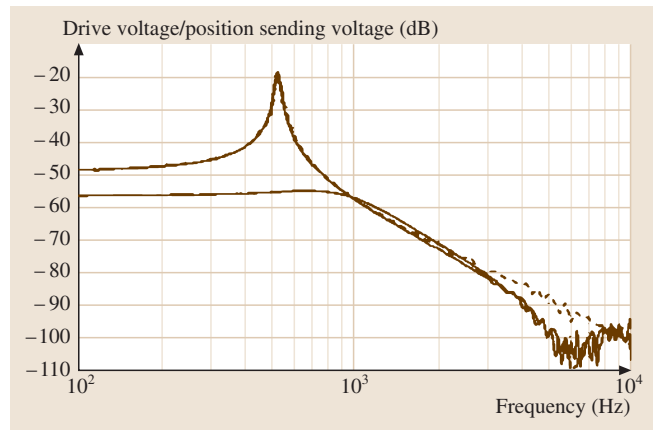


**Fig. 32.10** Open-loop and closed-loop frequency response of the prototype microactuator with a pico-slider. The capacitive position measurement (solid line) is compared to the measurements from LDV (dashed line). Courtesy from Naiuvudhi Wongkomet

age resulting from sensing error ( $V_{\text{error}}$ ), which appears at the output node of pre-amplifier, disappears from the voltage-input node to the buffer. Switches utilized in the circuit and their correspondent timing are shown in Fig. 32.9. Be aware that for presentation simplicity components in the pre-amplifier and buffer are not shown in detail in Fig. 32.9.

The frequency response, both open-loop and closed-loop with a PD controller, of the electrostatic microactuator measured by a capacitive position sensing circuit is shown in Fig. 32.10. The position measurements from an LDV are also shown in the same plot

for comparison. The deviation between measurements from the different position sensing devices appears in the high frequency region at the plot and has been identified as the feedthrough from the capacitance sensing circuit. The effect from feedthrough was negligible at low frequency region but becomes significant and results in a deviation in magnitude for the transfer function of  $-80\text{ dB} \sim -90\text{ dB}$  after 2 kHz. The feedthrough presented in the capacitance sensing circuits limited the position sensing resolution to the level of 10 nm.

## 32.2 Fabrication

While there are several approaches to building electrostatic microactuators suitable for hard disk drives, they all exhibit certain common features from a fabrication standpoint.

### 32.2.1 Basic Requirements

As we discussed earlier, nearly all electrostatic microactuators rely on a system of interlaced fingers or plates to provide actuation force. As a result, a method for producing arrays of these fingers or plates with narrow gaps between them is usually the central concern in developing a fabrication process. The resulting structure must then be strong enough to support both the slider on the microactuator and the microactuator on the suspension, particularly when loaded by the air-bearing that supports the slider above the hard drive's spinning disk. In addition, the design and fabrication process must include a way to perform electrical interconnection on the microactuator. This involves transferring signals to and from the actuator and slider and isolating the parts of the microactuator requiring different voltage levels.

In addition, the microfabrication process is subject to certain basic constraints. The materials used in fabrication must either be thermally and chemically compatible with any processing steps that take place after their deposition or must somehow be protected during steps that would damage them. This often constrains the choice of materials, deposition techniques, and processing order for many microdevices. Another concern is that the surface of the structure be planar within photoresist spinning capabilities and lithography depth-of-focus limits if patterning is to be performed. This can be a major challenge for disk drive microactuators, which are large

in size and feature high-aspect ratio trenches compared to other MEMS devices.

### 32.2.2 Electrostatic Microactuator Fabrication Example

Section 32.1.5 described the design and operation of a translational electrostatic microactuator. This section examines the fabrication process by which that microactuator was built [32.5]. The process is a variation on a micro-molding process known as HexSil [32.20]. In a micro-molding process, a mold wafer defines the structure of the microactuator and may be reused many times like dies in macro-scale molding; in the HexSil version of the procedure, the mechanical parts of the microactuator are formed in the mold by polysilicon. A second wafer is used to create metallized, patterned target dies. Upon extraction from the mold, the HexSil structure is bonded to this target substrate, which is patterned to determine which sections of the HexSil structure are electrically connected.

Naturally, the mold wafer is the first item to be processed and is quite simple. It is a negative image of the desired structure, etched down into the wafer's surface, as shown in Fig. 32.11a. A deep but very straight etch is critical for successful fabrication and subsequent operation of the devices. If the trench is too badly bowed or is undercut, the finished devices will be stuck in the mold and difficult to release. On the other hand, a tall device will have a larger electrostatic array area, will generate more force, and be better able to support a slider while in a disk drive.

Fabrication of the HexSil structure forms the majority of the processing sequence Fig. 32.11b–g. HexSil

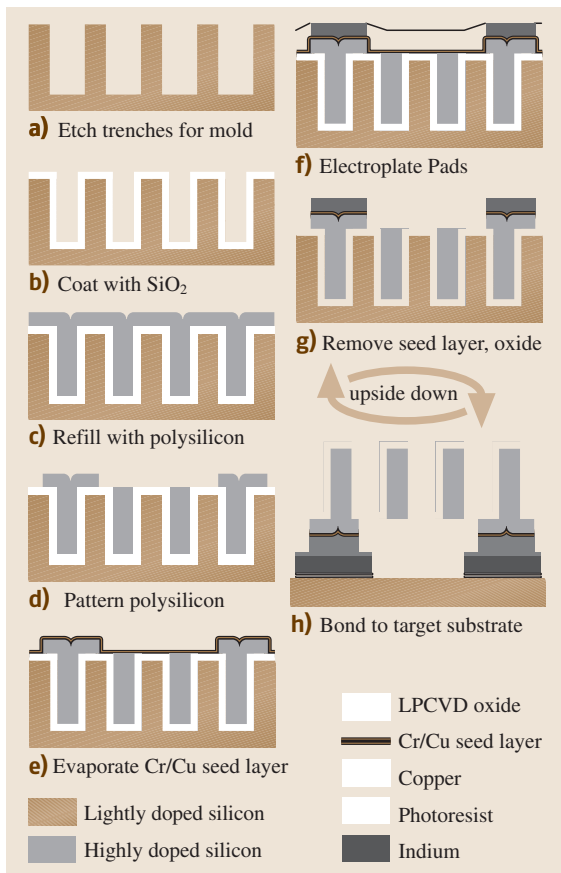


Fig. 32.11 Fabrication example 1: HexSil<sup>TS3</sup>

fabrication begins by coating the surface of the mold wafer with a sacrificial silicon oxide. This layer, deposited by low-pressure chemical vapor deposition (LPCVD), must coat all surfaces of the mold, so that removal of the oxide at the end of the process will leave the device completely free of the mold. This microactuator uses a 3 to 4 μm thick oxide layer to ensure clearance between the polysilicon structure and the trench walls during release. The mold is then refilled completely with LPCVD polysilicon, which will form the desired mechanical structure. Polysilicon is chosen for its conductivity and good conformality in refilling trenches. This also leaves a planar surface ready for photolithography to cover bonding locations. After the lithography step, the polysilicon deposited on top of wafer is removed, except where the bonding points were defined.

The structure is then prepared for bonding by forming a soldering surface. First a chrome/copper seed layer is evaporated on the surface of the wafer. The chrome promotes copper adhesion to the silicon, while the copper forms the starting point for electroplating. The seed layer is covered with photoresist, which is cleared only in the locations where contacts are desired. There, electroplating will produce a metal film, forming soldering points for the device to the target substrate that will form its base. In this case, copper is used as the plating material, thanks to its high conductivity and solderability. The device is released from the mold by ion milling away the thin seed layer, then dissolving the oxide lining with a hydrofluoric (HF) acid wet etch. The free standing portion of the microactuator is thus ready for bonding to the target. The mold, meanwhile, may be used again after a simple cleaning step.

The target substrate may be prepared in several ways. The target shown above consists simply of indium solder bumps and interconnects on a patterned seed layer; it is known as a “plating bus” arrangement. The seed layer is used for the same reasons as on the HexSil structure, but in this case the seed layer is patterned immediately, with the unwanted portions removed by sputter etching. This provides isolation where desired without having to etch the seed layer after the indium is in place. Photoresist is spun again and patterned to uncover the remaining seed layer. A layer of indium is then electroplated everywhere the seed layer is visible. Indium acts as the solder when the two parts of the microactuator are pressed together, forming a cold weld to the copper at 200–300 MPa that was found suitable for hard disk requirements, as shown in Fig. 32.11h.

### 32.2.3 Electrostatic Microactuator Example Two

The high-aspect ratio microactuator described in this section is in development at the University of California, Berkeley, and demonstrates another way to create the features required of an actuated slider. The microactuator is translational, with parallel-plates actuation, and includes two of the design options described previously: integrated isolation plugs, as described in Sect. 32.1.3, and a capacitive sensing array, as described in Sect. 32.1.4. A picture of the basic design is shown in Fig. 32.12; a central shuttle holding the slider is supported by four folded-flexure springs and driven by parallel-plates arrays.

Basic Process: Silicon-on-Insulator

TS<sup>3</sup> In the manuscript we couldn't see different colors for LPCVD oxide, copper and photoresist. Please show what is what in the draw.

TS<sup>3</sup> In the manuscript we couldn't see different colors for LPCVD oxide, copper and photoresist. Please show what is what in the draw.

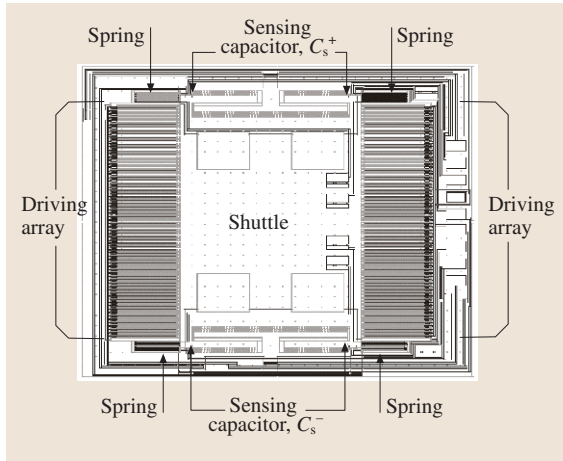


**Fig. 32.12** Translational high-aspect ratio microactuator

Successful processing of the design is centered around the ability to etch very straight, narrow trenches using deep reactive ion etching (DRIE). DRIE is a special plasma etching sequence that uses polymerization of the sidewalls of a trench to keep the walls straight even at extreme aspect ratios. Deep, narrow trenches make possible a microactuator with both closely packed electrostatic arrays and good mechanical strength. Conventional surface micromachining is used to produce the majority of the electrical interconnects.

The basic fabrication process uses a silicon-on-insulator (SOI) wafer to control DRIE trench depth. SOI wafers are very useful in microfabrication as they provide a layer of single-crystal silicon (the device layer) separated from the bulk of the wafer (the handle layer) by a thin layer of buried silicon oxide. This gives a very well controlled thickness to finished device but is very expensive. The microactuators described here are fabricated from an SOI wafer with a  $100\ \mu\text{m}$  device layer. A variation on the processing sequence and layout eliminates the need for SOI wafers and will be discussed in the following section.

The first stage of fabrication is creation of deep isolation trenches (see Fig. 32.13a–c). This procedure has been adapted to MEMS from integrated circuit processing for isolating thick MEMS structures [32.21]. The isolation pattern is formed by photolithography and etched by DRIE down to the buried oxide. With trenches only  $2\ \mu\text{m}$  wide, this corresponds to an aspect ratio of 50 : 1. The wafer surface and trenches are then coated with LPCVD silicon nitride, which acts as the electrical insulator. The trench is then refilled in its entirety

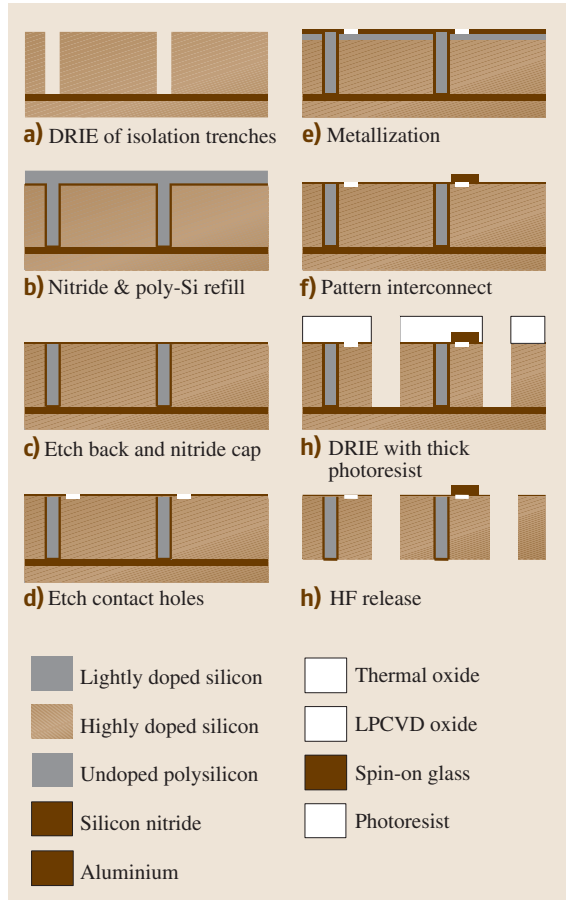


**Fig. 32.13** Basic silicon-on-insulator fabrication process<sup>TS3</sup>

with LPCVD polysilicon, that a more conformal material better fills the trench than silicon nitride would alone; polysilicon also has much lower residual stresses than silicon nitride. The refill leaves a layer of polysilicon on the surface of the substrate, which must be etched or polished back to the silicon nitride. After etch-back, a second layer of LPCVD nitride completes isolation between regions.

Next, electrical interconnects are formed, as shown in Fig. 32.13d–f. Contact holes to the substrate are defined by photolithography and etched by reactive ion etching of the silicon nitride. Metal lines may then be patterned directly by photolithography or formed by lift-off. In a lift-off process, photoresist is deposited and patterned before the metal. The metal is then deposited vertically, so that the sidewalls of the resist are uncovered. Dissolving the resist allows the metal on top to

float away, leaving behind the interconnect pattern. In the figures shown here, the interconnects are formed by evaporated aluminum, eliminating the need for electroplating and a seed layer. The ability to isolate portions of the substrate is useful for simplifying the interconnect layout, as one interconnect can cross another by passing underneath it through an isolated portion of the substrate.

Finally, structural lithography is performed and a second etch by DRIE is done, as shown in Fig. 32.13g. These trenches will define the shape of the microactuator, and are larger,  $4\ \mu\text{m}$  wide, to allow sufficient rotor travel. After this etch step, the device layer on the SOI buried oxide consists of fully defined microactuators. When the buried oxide is removed by wet etching, the microactuator is released from the substrate Fig. 32.13h and, after removal of the photoresist that protected the device surface from HF during release, ready for operation. Thanks to the high-aspect ratios of DRIE and the efficient integrated isolation scheme, the microactuator can theoretically be operated with a DC bias voltage of 15 V on the rotor, and a dynamic stator voltages below 5 V. In practice, higher voltages are required due to the spreading of trench walls over the course of DRIE. A picture of the electrostatic structure, with the rotor fingers on the left and the stator fingers on the right, divided down the center by isolation trenches, is shown in Fig. 32.14.

#### Variation: Anisotropic Backside Release

An alternative fabrication approach is to build the microactuator from a regular silicon wafer ( $\sim 550\ \mu\text{m}$  thick), but then, since the microactuator shouldn't be more than  $100\ \mu\text{m}$  thick to fit in a HDD, etch away the backside of the wafer to obtain devices of that size. The main reason for using a silicon-only wafer is to reduce the need for

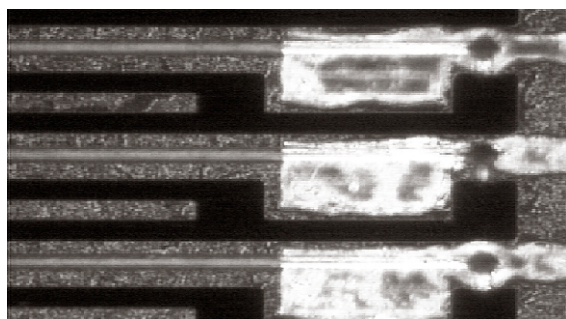


**Fig. 32.14** Electrostatic driving array of microactuator from SOI

expensive SOI wafers, which cost approximately ten times as much as single-material wafers. Another benefit is the elimination of the need for etch holes to reach the buried oxide layer, which increase vulnerability of microactuators to particle or moisture contamination. But, the thickness of the devices cannot be controlled as accurately as with the SOI process, and the processing sequence is more complicated.

Control of backside etching is difficult, making it hard to obtain devices with uniform thickness across a wafer. A proposed solution is to use an anisotropic wet etchant during the backside etch step. Anisotropic etchants work very slowly on certain crystal planes of a single-crystal silicon wafer; a coating on trench sidewalls can protect fast-etching planes when the etchant reaches the trenches from the back, causing slow-etching crystal planes to begin coming together slowing the etch. The result is a nearly self-stopping etch with a V-shaped profile that prevents overetching even in the presence of nonuniformities in etch rate and trench depth across the wafer. The most common anisotropic etchants are potassium hydroxide (KOH) and tetramethyl ammonium hydroxide (TMAH). This release process is referred to here as an anisotropic backside release (ABR).

The key to a good release by this method is to achieve excellent protection of the top of the wafer and the deep trenches from the etchant, and this necessitates changes in the process flow from that for an SOI wafer. Without a good protective film, the interconnects on the surface of the wafer could be destroyed, or the fast-etching planes might be attacked along the trench sidewalls. Of the etchants mentioned above, TMAH is preferred, due to high selectivity to both silicon oxide and nitride and, especially, thermally grown oxide, which can be used as protective films. But, growing thermal oxide and/or depositing high-quality nitride are high temperature processes not compatible with most metals, so the structural trenches must be etched and oxidized before forming the electrical interconnects. As shown in Fig. 32.15c–d, the isolation trenches are formed as before, but the structural trenches are patterned and etched in the very next step. A thermal oxide is then grown in the trenches to produce the protective oxide layer Fig. 32.15e.

To do lithography for the interconnects at this point, then, the surface of the wafer must be planarized. This is done by refilling the trenches with spin-on-glass. The spin-on-glass plugs the trenches nearly to the top and can be sacrificed along with the thermal oxide at the end of the process. Extra glass on the wafer surface can be removed by a quick HF dip or chemical mechanical polishing. The resulting surface is uneven, as shown

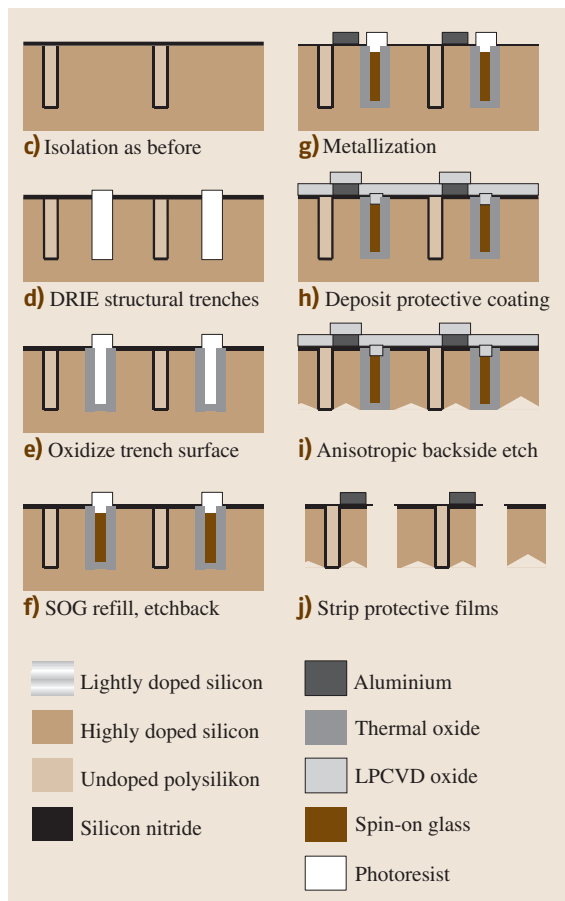


**Fig. 32.15** Deep trench fabrication process adapted for backside release<sup>TS3</sup>

in Fig. 32.15f, but a thick photoresist layer can be applied over the trenches evenly enough to accomplish contact and metal patterning lithographies. After metallization much the same as for the SOI wafer Fig. 32.15g, a final coating of etch resistant material is required to protect the metal during backside release, as shown in Fig. 32.15h–j. After ABR, the backside of the device will be shaped by crystal planes, but the thickness of the device at the edge of DRIE features will be fixed. While a combination of silicon oxide and silicon nitride has been effective over a “metallization” of undoped polysilikon, an effective combination of true metal interconnects and protective films has yet to be found and is an ongoing area of research for improving the ABR process sequence.

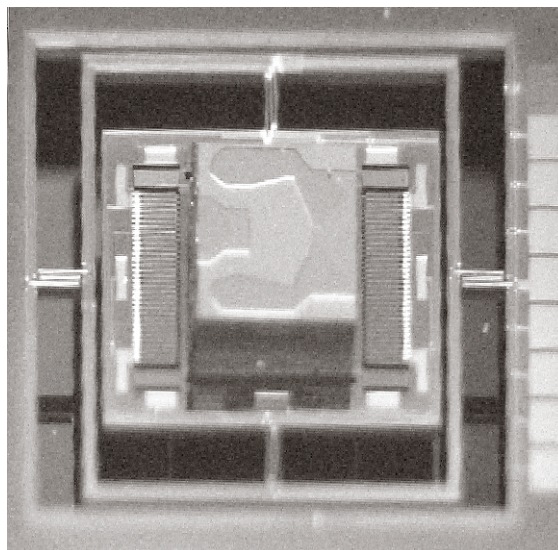


**Fig. 32.16** Microactuator with integrated gimbal fabricated by ABR

A prototype microactuator with integrated gimbal fabricated using ABR is shown in Fig. 32.16. This prototype was operated with a 30 V DC bias and  $\pm 8$  V AC driving voltage for  $\pm 1 \mu\text{m}$  displacement, while a larger version (shown in Fig. 32.12<sup>TS4</sup>) was operated at 15 V bias and  $\pm 3$  V driving. This layout and fabrication concept is currently being adjusted to fit a MEMS-ready suspension for more advanced testing.

### 32.2.4 Other Fabrication Processes

Where the DRIE-based process described above “digs” the microactuator out of a wafer, a procedure developed by IBM “grows” a microactuator with high-aspect ratio trenches on top of a wafer [32.22].

#### IBM Electroplated Microactuator

This is done by a clever sequence of electroplating steps and sacrificial depositions. An oxide sacrificial film is first patterned then covered with a metal seed layer. When later removed, the sacrificial will have left a gap between the microactuator and substrate portions of the microactuator needed to move freely. A polymer,  $40 \mu\text{m}$  thick, is spun onto the wafer and patterned with a reverse image of the main structural layer. Trenches are etched down to the sacrificial layer by plasma etching then refilled by electroplating, much like micro-molding. An-

<sup>TS4</sup> Is Fig. 32.12 here correct?

other sacrificial polymer, photoresist this time, separates the top of the fixed portions of the structure from the platform upon which the slider will sit, while conveniently planarizing the surface for further lithography. The platform is created by two more electroplating steps on top of the parts of the structure that will move freely. Removal of the sacrificial layers (photoresist, polymer, and oxide) releases the microactuator for use.

This process has been used to produce both rotary and linear microactuators and is comparatively advanced from a commercial standpoint. The resulting devices are thinner than those described in the previous example, but a similar aspect ratio (20 : 1) can be achieved. This procedure also has the benefits of being a low temperature process, which helps decrease processing cost and is compatible with the thin film magnetic head manufacturing process. Moreover it includes an upper structure that covers the fingers, which improves device reliability by shielding the fingers from particles.

Additional fabrication details and dynamic testing results for the IBM design may be found in references [32.22] and [32.23]. Certain control results are described in Sect. 32.3.2.

#### Electroplated Microactuators with Fine Gaps

Finally, fabrication processes developed at the University of Tokyo demonstrate additional techniques for obtaining very small gaps between electrostatic fingers [32.24]. Similar to the IBM process, electrostatic fingers are electroplated, in this case by nickel, within a polymer pattern. The gap between closely spaced fingers, however, is then formed by a sacrificial metal. Photoresist is used to cover the fingers except for the surfaces where a small gap is desired; these are electroplated with sacrificial copper, making narrow, well-defined gaps possible, in perhaps the most reliable of the processes described here. Continuing with a second nickel electroplating step creates the interlaced fingers, which will also support the slider; the wafer is polished down to level the structure. Finally the copper, photoresist, and seed layer are etched away, leaving the free standing structure.

In another version of process, photoresist alone separates the stator and rotor fingers. In this case, a thin layer of photoresist is left where small gaps are desired, instead of growing a layer of copper. This method is dependent on excellent alignment but can eliminate the need for polishing after the second electroplating step.

### 32.2.5 Suspension-Level Fabrication Processes

The long, highly integrated fabrication processes required by actuated slider microactuators contrast greatly with the fabrication of actuated suspension microactuators.

#### PZT Actuated Suspensions

In most cases, actuated suspensions use piezoelectric (PZT) drivers cut or etched as single, homogeneous pieces and attached to the steel suspension. Nevertheless, microfabrication techniques can still be useful in suspension processing. For example, some recent suspensions have used thin film PZT deposited on a substrate by sputtering for incorporation in a suspension. This is intended to produce a higher quality PZT films and begins to introduce MEMS-style processing techniques even into suspension-scale manufacturing [32.25, 26].

#### Integrated Silicon Suspension

Another area where silicon processing has been suggested for use on a suspension is the gimbal region, or even the entire suspension, as described in [32.19]. An integrated silicon suspension would incorporate aspects of both actuated suspension and actuated slider fabrication. Force is provided by four piezes of bulk PZT cut down to size, as in other actuated suspensions, but the rest of the suspension is fabricated from single-crystal silicon by bulk micromachining.

The fabrication process for the integrated suspension is the precursor to the ABR process used to fabricate the microactuator in Sect. 32.2.3. Layers of LPCVD silicon nitride and polysilicon are deposited on a bare silicon wafers. The polysilicon is doped by ion implantation and covered with a second layer of nitride. The outline of the suspension and any spaces within it are then lithographically patterned. After a reactive-ion nitride etch to reach the substrate, trenches are etched by DRIE. The trenches are then plugged with spin-on-polymer for further lithography. First, the top layer of polysilicon is patterned into piezoresistive strips for sensing vibration. Second, a layer of photoresist is patterned for copper lift-off, to create metal interconnects. Last, the planarizing polymer is removed, and the entire surface is coated with silicon nitride. This final coating protects the top surface during an anisotropic backside wet etch, in this case by potassium hydroxide.

#### Instrumented Suspensions

Finally, microfabrication techniques may be useful for installing sensors on conventional steel suspensions. The concept is to deposit a dielectric and a piezoresistive material on the stainless steel sheet that will be formed into the central piece of the suspension and will pattern piezoresistors directly by lithography and plasma etching. A second lithography may be used to add metal lines back to the E-block. Vibration sensors on the suspension are very desirable for controlling slider position, and the use of thin-film deposition and photolithography permits the sensors to be located at the points most effective for detecting vibration. An example of a sensor formed by this method is shown in Fig. 32.17.

### 32.2.6 Actuated Head Fabrication

Several interesting fabrication processes have been proposed for another approach to creating a dual-stage disk drive servo: the actuated head. In an actuated head, the actuator is built into the slider and moves just the read/write head. This could potentially eliminate many of the mechanical limits of actuated suspensions or actuated sliders. Actuation techniques are typically similar to those of actuated sliders, with the key complication being the need to integrate an actuator fabrication process with a slider fabrication process. We discuss ways in which this might be done below.

One fabrication approach to actuating a read/write head is to enclose an electrostatic driving array inside a slider. The slider is built on a glass or silicon substrate, beginning with the air-bearing surface (ABS), followed by a microactuator, and then surrounded by the remainder of the slider. The ABS is formed by silicon oxide deposited over aluminum and tapered photoresist layers that give it a contoured shape. The majority of the ABS is then covered with photoresist, while a block in the center is plated with nickel and etched to form the electrostatic actuator. The electrostatic microactuator, in turn, is covered while the remainder of the slider body is electroplated. The slider may then be bonded to a suspension and the ABS surface released from the substrate by etching away the original aluminum and photoresist surface [32.9].

The sacrificial metal technique described in Sect. 32.2.4 is another possibility for building an elec-



Fig. 32.17 Piezoresistive strain sensor on steel substrate

trostatic array onto a slider. It can be used to form small array with very narrow gaps, and the process is compatible with slider and head materials [32.27].

The third actuated-head process makes use of an SOI wafer and silicon based materials. For this structure, a 20  $\mu\text{m}$  device layer is coated with silicon nitride. The nitride is patterned with contact holes for connections to the substrate and used as insulation over the rest of the device. A layer of molybdenum is sputter deposited to perform interconnections to both the head and the electrostatic array. This array is formed by DRIE to the buried oxide, using a lithographically patterned hard mask of tetraethylorthosilicate. The result is a simple, tiny, actuator that must be bonded to the edge of a slider after release from the SOI wafer [32.28].

## 32.3 Servo Control Design of MEMS Microactuator Dual-Stage Servo Systems

The objective of disk drive servo control is to move the read/write head to the desired track as quickly as

possible, referred to as track seek control, and, once on-track, position the head on the center of the track as precisely as possible, referred to as track-following control, so that data can be read/written quickly and reliably. The implementation of the servo controller relies on the position error signal (PES), which is obtained by reading the position information encoded on the disk's data tracks.

### 32.3.1 Introduction to Disk Drive Servo Control

The position error is also called track mis-registration (TMR) in the disk drive industry. Major TMR sources in the track-following mode include spindle runout, disk fluttering, bias force, external vibration/shock disturbance, arm and suspension vibrations due to air turbulence, PES noise, written-in repeatable runout, and residual vibration due to seek/settling [32.29]. These sources can be categorized as runout,  $r$ , input disturbance,  $d$ , and measurement noise,  $n$ , by the locations they are injected into the control system, as shown in Fig. 32.18. In Fig. 32.18,  $G_P(s)$  and  $G_C(s)$  represent the disk drive actuator and the controller, respectively;  $r$  and  $x_p$  represent track runout and head position, respectively.

From Fig. 32.18, the *PES* can be written as

$$PES = S(s)r + S(s)G_P(s)d - S(s)n, \quad (32.9)$$

where  $S(s)$  is the closed loop sensitivity function defined by

$$S(s) = \frac{1}{1 + G_C(s)G_P(s)}. \quad (32.10)$$

The higher the bandwidth of the control system, the higher the attenuation of the sensitivity function  $S(s)$  below the bandwidth. Thus, one of the most effective methods to reduce *PES* and increase servo precision is to increase the control system bandwidth.

Traditional disk drive servo systems utilize a single voice coil motor (VCM) to move the head. Multiple structural resonance modes of the E-block arm and the suspension located between the pivot and the head impose a major limitation on the achievable control bandwidth. A dual-stage servo system using a MEMS actuated-slider microactuator can achieve high bandwidth because the microactuator is located between the suspension and the slider, thus by-passing the pivot, E-block arm, and suspension resonance modes.

One basic task of dual-stage servo control design is to increase control bandwidth using the second stage actuator. Many design methodologies have been developed to accomplish this objective. In this section, we first review major dual-stage servo control design methodologies, and then we discuss design considerations for controller design of a MEMS microactuator dual-stage servo system. As design examples, the details of track-following control designs using a sensitivity function decoupling design method and the  $\mu$ -synthesis design method are presented in Sect. 32.3.3. In Sect. 32.3.4,

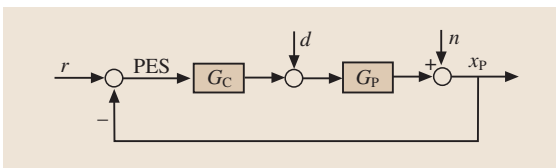


Fig. 32.18 Disk drive servo control

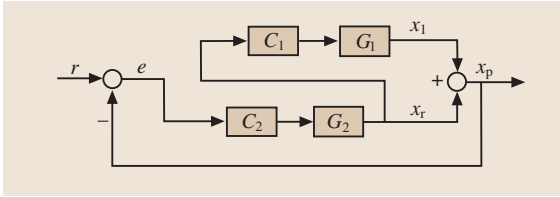


Fig. 32.19 Master-slave design structure

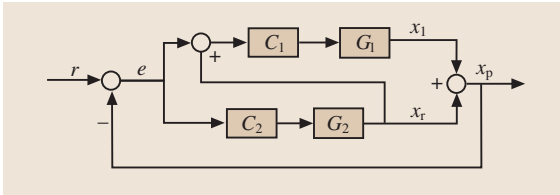


Fig. 32.20 Decoupled control design structure

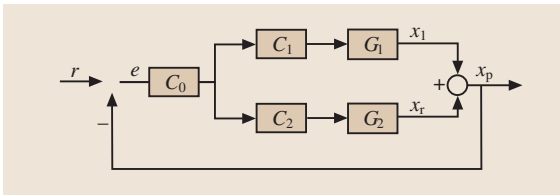


Fig. 32.21 PQ control design structure

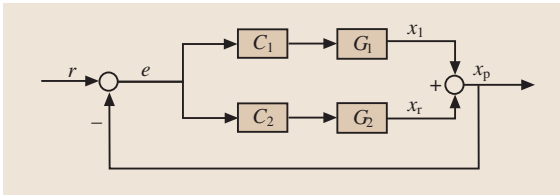


Fig. 32.22 Parallel control design structure

we introduce a short-span seek control scheme using a dual-stage actuator based on decoupled feed forward reference trajectories generations.

### 32.3.2 Overview of Dual-Stage Servo Control Design Methodologies

Various control design architectures and methodologies have been developed for dual-stage servo control design. They can be largely classified into two categories: those based on decoupled or sequential single-input-single-output (SISO) designs, and those based on modern optimal design methodologies, such as LQG, LQG/LTR,

$H_\infty$ , and  $\mu$ -synthesis, in which the dual-stage controllers are obtained simultaneously.

Two constraints must be considered in dual-stage servo control design. First, the contribution from each actuator must be properly allocated. Usually the first stage actuator, or the coarse actuator, has a large moving range but a low bandwidth while the second stage actuator, or the fine actuator, has a high bandwidth but small moving range. Second, any destructive effect, in which the two actuators fight each other by moving in opposite directions, must be avoided.

#### Classical SISO Design Methodologies

Several architectures and design methodologies have been proposed to transform the dual-stage control design problem into decoupled or sequential multiple SISO compensators design problems, for example, master-slave design, decoupled design [32.30], PQ method [32.31], and direct parallel design [32.32]. Figure 32.19 to 32.22 shows the block diagrams of dual-stage controller designs using these methods. In these figures,  $G_1$  and  $G_2$  represent the coarse actuator (VCM) and fine actuator (microactuator) respectively;  $x_1$  is the position of the coarse actuator;  $x_r$  is the position of the fine actuator relative to the coarse actuator;  $x_p$  is the total position output;  $r$  is the reference input (runout), and  $PES$  is the position error,  $e = r - x_p$ .

**Master-slave Design.** In a traditional master-slave structure, the absolute position error is fed to the fine actuator, and output of the fine actuator is fed to the coarse actuator, as shown in Fig. 32.19. The position error will be compensated by the high bandwidth fine actuator. The coarse actuator will follow the fine actuator to prevent its saturation.

**Decoupled Design.** Figure 32.20 shows the decoupled design structure [32.30], which is similar to the master-slave structure. Instead of feeding just the fine actuator output to the coarse actuator, however, the summation of the fine actuator output and the position error is fed, which equals the position error of the coarse actuator. A very nice feature of this structure is that the control system is decoupled into two independent control loops, and the total sensitivity function is the product of the sensitivity functions of each of the control loops [32.13]. Thus the two compensators  $C_1$  and  $C_2$  can be designed independently. Decoupled design is also called decoupled master-slave design, or sensitivity function decoupling design. In Sect. 32.3.3, we will

discuss details of a track-following controller designed using this method.

Both the master-slave and the decoupled designs use the relative position of the fine actuator,  $x_r$ . If a relative position sensor is unavailable,  $x_r$  can be estimated using a model of the fine actuator.

**PQ Design Method.** The PQ method is another innovative design technique for control design of dual-input, single-output system [32.31]. A block diagram of a dual-stage control design using this method is shown in Fig. 32.21.

In PQ design,  $P$  is defined by

$$P = \frac{G_1}{G_2}, \quad (32.11)$$

and a dual-stage controller can be designed in two steps. The first involves the design of an auxiliary compensator  $Q$  for plant  $P$ , which is defined by

$$Q = \frac{C_1}{C_2}. \quad (32.12)$$

$Q$  is designed to parameterize the relative contribution of the coarse and fine actuators. The 0 dB crossover frequency and phase margin of the open loop transfer function  $PQ$  are the design parameters in the design of  $Q$ . At frequencies below the 0 dB crossover frequency of  $PQ$ , the output is dominated by the coarse actuator, while at frequencies above the 0 dB crossover frequency, the output is dominated by the fine actuator. At the 0 dB crossover frequency, the contributions from the two actuators are equal. A large phase margin of  $PQ$  will ensure that the two actuators will not fight each other when their outputs are close in magnitude, thus avoiding any destructive effects.

The second step in the  $PQ$  design methodology is to design a compensator  $C_0$  for SISO plant  $PQ$  such that the bandwidth (crossover frequency), gain margin, phase margin, and error rejection requirements of the overall control system are satisfied.

**Direct Parallel Design.** It is also possible to design the dual-stage controller directly using a parallel structure, as shown in Fig. 32.22, by imposing some design constraints and by sequential loop closing [32.32].

The two constraints for parallel design in terms of the  $PES$  open loop transfer functions are [32.32]:

$$C_1(s)G_1(s) + C_2(s)G_2(s) \rightarrow C_2(s)G_2(s), \quad (32.13)$$

at high frequencies and

$$|C_1(s)G_1(s) + C_2(s)G_2(s)| \gg |C_2(s)G_2(s)|, \quad (32.14)$$

at low frequencies. The first constraint implies that open loop frequency response of the dual-stage control system at high frequencies approximately equals that of the fine actuator control loop. Thus the compensator  $C_2(s)$  can be first designed independently as a SISO design problem to satisfy the bandwidth, gain margin, and phase margin requirements of the dual-stage control system. Compensator  $C_1(s)$  can then be designed for the SISO plant model with the fine actuator control loop closed, such that the low frequency constraint and overall stability requirement are satisfied. This model is defined by:

$$G(s) = \frac{G_1(s)}{1 + C_2(s)G_2(s)}. \quad (32.15)$$

A dual-stage controller for a MEMS dual-stage actuator servo system has been designed using this method and implemented at IBM. An open loop gain crossover frequency of 2.39 kHz with gain margin 5.6 dB and phase margin 33° was obtained. In experimental testing, a 1- $\sigma$  TMR of 0.024  $\mu\text{m}$  has been achieved [32.32].

### Modern MIMO Design Methodologies

Since the dual-stage actuator servo system is a MIMO system, it is natural to utilize modern MIMO optimal design methodologies, such as LQG, LQG/LTR,  $H_\infty$ , and  $\mu$ -synthesis, to design the dual-stage controller. Usually MIMO optimal designs are based on the parallel structure shown in Fig. 32.22, augmented with noise/disturbances models and other weighting functions to specify the control design performance objectives.

Linear quadratic Gaussian (LQG) control combines a Kalman filter and optimal state feedback control based on the separation principle. But, the Kalman filter weakens the desirable robustness properties of the optimal state feedback control. Linear quadratic Gaussian/loop-transfer recovery (LQG/LTR) control recovers robustness by a Kalman filter redesign process. Dual-stage control designs using LQG and LQG/LTR have been reported in [32.33–35], and so on.

The LQG design methodology minimizes the  $H_2$  norm of the control system, while the  $H_\infty$  design methodology minimizes the  $H_\infty$  norm of the control system.  $\mu$ -synthesis design methodology is based on the  $H_\infty$  design and accounts for plant model uncertainties during the controller synthesis process with guaranteed robustness. Dual-stage control designs based on the  $H_\infty$  and  $\mu$ -synthesis design methodologies have been reported in [32.33, 36, 37], and so on. Some details of a control design using  $\mu$ -synthesis for the MEMS micro-

actuator dual-stage servo system will be presented in Sect. 32.3.3

Other advanced control theories also have been applied to dual-stage servo control designs, such as sliding mode control [32.38], neural networks [32.39], and so forth.

### 32.3.3 Track-Following Controller Design for a MEMS Microactuator Dual-Stage Servo System

MEMS microactuators for dual-stage servo application are usually designed to have a single flexure resonance mode between 1–2 kHz [32.8,40]. This resonance mode is usually very lightly damped and can have a  $\pm 15\%$  variations due to the differences in the fabrication processes. Since the uncertain resonance frequency is relatively low and close to the open loop gain crossover frequency of the control system, robustness to these variations must be considered in the controller design.

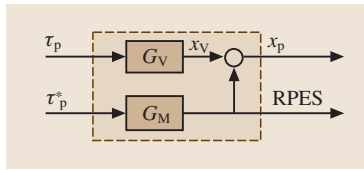


**Fig. 32.23** Dual-stage control plant

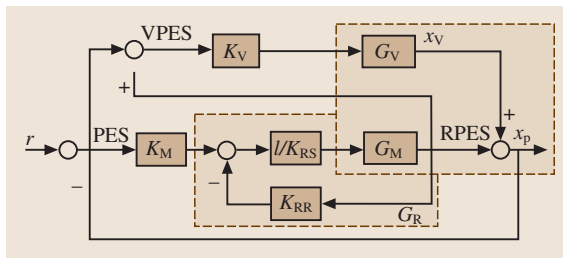


**Fig. 32.24** Decoupled dual-stage control design block diagram

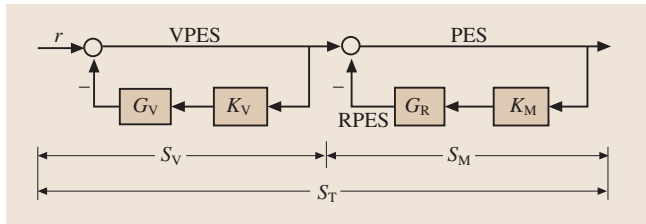


**Fig. 32.25** The sensitivity block diagram

### Controller Design Considerations for MEMS Microactuator Dual-stage Servo System

Capacitive sensing can be utilized in MEMS microactuators to measure the position of the microactuator relative to the VCM actuator [32.14, 40]. But, this requires additional sensing electronics and wires to and from the head gimbal assembly (HGA), which result in additional fabrication and assembly costs. Thus whether or not a relative position sensor will be used in MEMS dual-stage servo systems is still an open question. If the microactuator’s resonance mode is lightly damped, it is susceptible to airflow turbulence and external disturbances. The relative position signal can be utilized to damp the microactuator’s resonance mode. Dual-stage control can be classified as MIMO or SIMO designs according to the availability of the relative position signal.

Given the fact that the inertia of the MEMS microactuator is very small compared to that of the VCM, the effect of the motion of the microactuator on the VCM can be neglected. By feeding the control input of the VCM to the input of the microactuator with a proper gain, we can cancel the coupling effect of the VCM on the microactuator [32.13]. Thus the dual-stage control model can be decoupled as the sum of the outputs of the VCM and the microactuator, as shown in Fig. 32.23, in which  $G_V$ ,  $G_M$  are the VCM and microactuator models respectively, and  $x_p$  is the absolute position of the read/write head, which equals the absolute position of the VCM,  $x_v$ , and the position of the microactuator relative to the VCM,  $RPES$ .

### Decoupled Track-Following Control Design and Self-Tuning Control

Figure 32.24 shows a block diagram used for decoupled control design of MEMS microactuator dual-stage servo systems [32.13].

#### Sensitivity Function Decoupling Design Methodology.

The part enclosed in the dashed box on the upper-right corner is the dual-stage plant model shown in Fig. 32.23. In the figure,  $G_V$  and  $G_M$  are the VCM and microactuator models, respectively;  $x_p$  is the absolute position of the read/write head;  $x_v$  is the absolute position of the VCM actuator; and  $RPES$  is the position of the microactuator relative to the VCM;  $r$  represents the track runout, and  $PES$  is the position error signal of the head relative to the data track.

The decoupling control approach, originally introduced in [32.30], utilizes the  $PES$  and  $RPES$  signals to generate the position error of the VCM relative to the

data track center, labeled as  $VPES$ ,

$$VPES = PES + RPES = r - x_v, \quad (32.16)$$

and this signal is fed to the VCM loop compensator.

As shown in the block diagram, three compensators need to be designed: the VCM loop compensator  $K_V$ ; the microactuator  $PES$  loop compensator  $K_M$ ; and the microactuator  $RPES$  minor loop compensator  $K_{MM} = K_{RR}/K_{RS}$ , which is used to damp the microactuator's flexure resonance mode and place the closed loop poles of the microactuator  $RPES$  loop at appropriate locations. The damped microactuator closed loop transfer function  $G_R$ , shown in the lower-middle dashed box, is defined by

$$G_R = \frac{G_M}{K_{RS} + G_M K_{RR}}, \quad (32.17)$$

while the total dual-stage open loop transfer function from  $r$  to  $x_P$ ,  $G_T$ , is

$$G_T = K_V G_V + K_M G_R + K_M G_R K_V G_V. \quad (32.18)$$

It can be shown that the block diagram in Fig. 32.24 is equivalent to the sensitivity block diagram shown in Fig. 32.25, and the total closed loop sensitivity function from  $r$  to  $PES$  equals the product of the VCM and microactuator loop sensitivities,  $S_V$  and  $S_M$ , respectively:

$$S_T = \frac{1}{1 + G_T} = S_V S_M, \quad (32.19)$$

where

$$S_V = \frac{1}{1 + K_V G_V}, S_M = \frac{1}{1 + K_M G_R}. \quad (32.20)$$

Thus the dual-stage servo control design can be decoupled into two independent designs: the VCM loop and the microactuator loop design. The VCM loop sensitivity can be designed using traditional single-stage servo design methodologies. The microactuator loop sensitivity is designed to expand the bandwidth and increase the attenuation of low frequency runout and disturbances.

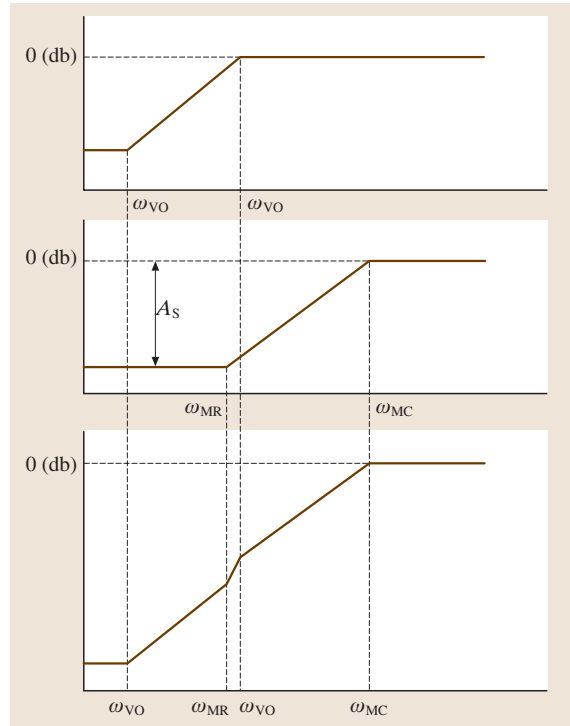


Fig. 32.26 Illustration of dual-stage sensitivity  $S_T$  design

**Closed Loop Sensitivity Design by Pole Placement.** For a typical sampled second order system with the discrete time transfer function

$$G(q^{-1}) = \frac{q^{-1} B_o(q^{-1})}{A_o(q^{-1})}, \quad (32.21)$$

where  $q^{-1}$  is one step delay operator;  $B_o(q^{-1})$  is the plant zero polynomial, and  $A_o(q^{-1}) = 1 + a_1 q^{-1} + a_2 q^{-2}$  is the plant pole polynomial. The closed loop sensitivity function can be designed by pole placement, solving the following Diophantine equation [32.41]:

$$A_c(q^{-1}) = A_o(q^{-1}) S(q^{-1}) + q^{-1} B_o(q^{-1}) R(q^{-1}), \quad (32.22)$$

where  $A_c(q^{-1})$  is the desired closed loop characteristic polynomial. The closed loop sensitivity function,  $G_S$ , is

$$G_S(q^{-1}) = \frac{A_o(q^{-1}) S(q^{-1})}{A_c(q^{-1})}, \quad (32.23)$$

and the discrete time controller  $C(q^{-1})$  is

$$C(q^{-1}) = \frac{R(q^{-1})}{S(q^{-1})}. \quad (32.24)$$

$A_c(q^{-1})$  can be chosen such that the required bandwidth and system response are satisfied. Usually it is more intuitive to describe it with its continuous time equivalent parameters: the damping ratio,  $\zeta$ , and the natural frequency,  $\omega_n$ . The damping ratio is directly related to the phase margin of the open loop transfer function. For a typical design, it can be chosen to be equal to or greater than one, in order to ensure adequate phase margin.  $\omega_n$  is related to the control system's bandwidth, which is limited by sampling frequency and time delay, or the high frequency structural dynamics of the system.

**Dual-Stage Sensitivity Function Design.** The compensators in the dual-stage servo system depicted in Fig. 32.24 can be designed by a two-step design process, as illustrated in Fig. 32.26.

First, the VCM loop compensator  $K_V$  is designed to attain a desired VCM closed loop sensitivity  $S_V$ , as shown in the top part of Fig. 32.26. Its bandwidth,  $\omega_{VC}$  in Fig. 32.26, is generally limited by the E-block and suspension resonance modes. The design of this compensator can be accomplished using conventional SISO frequency shaping techniques.

The second step of the design process involves the design of the microactuator loop compensators to attain additional attenuation  $S_M$ , as shown in the middle part of Fig. 32.26. This step is itself accomplished in two steps. First, the minor *RPES* loop compensator,  $K_{RR}/K_{RS}$ , is determined in order to damp the microactuator resonance mode and place the poles of  $G_R$ , or equivalently  $\omega_{MR}$  in Fig. 32.26, at desired locations. The

compensator can be obtained by solving a Diophantine equation by pole placement as discussed in the previous subsection. The poles of  $G_R$  will become the zeros of the microactuator loop sensitivity function,  $S_M$ .

Finally, the *PES* loop compensator  $K_M$  is designed to place the poles, or equivalently,  $\omega_{MC}$  in Fig. 32.26, of the microactuator loop closed loop sensitivity  $S_M$ .  $\omega_{MC}$  is limited by the *PES* sampling frequency and computational time delay [32.42].

The total dual-stage sensitivity is shown in the bottom part of Fig. 32.26. For a given  $\omega_{MC}$ , the additional attenuation  $A_S$ , provided by the microactuator loop, will be determined by  $\omega_{MR}$ . In our proposed procedure, the initial value of  $\omega_{MR}$  can be chosen to be the same as  $\omega_{VC}$ . It is then adjusted so the desired attenuation and phase margin requirements of the overall dual-stage system are satisfied. Decreasing  $\omega_{MR}$  increases the low frequency attenuation of the closed loop sensitivity function  $S_T$  but also generally reduces the phase margin of open loop transfer function  $G_T$ .

For SIMO design when the *RPES* is not available, the microactuator model can be used as an open loop observer to estimate the *RPES*. The combination of the open loop observer and the minor loop compensator is equivalent to a notch filter.

**Self-Tuning Control to Compensate Variations in the Microactuator's Resonance Mode.** An adaptive control scheme can be combined with the decoupled discrete time pole placement design methodology described above to compensate variations in the microactuator's resonance mode by tuning the microactuator *RPES* inner loop compensator.

A block diagram for the microactuator inner loop self-tuning control is shown in Fig. 32.27. The parameter adaptation algorithm (PAA) is a direct self-tuning algorithm, based on the microactuator inner loop pole placement design.

Consider the microactuator open loop transfer function in (32.21). Since the microactuator's resonance mode is lightly damped, the zero of the microactuator's discrete time transfer function is very close to 1 ( $z_o \approx 1$ ). Thus it is possible to factor out the "known" term ( $1 + z_o q^{-1}$ ) from the Diophantine equation (32.22). The resulting *RPES* minor-loop closed loop dynamics is given by

$$A_c(q^{-1})y(k) = q^{-1}b_0(1 + z_o q^{-1}) \times [K_{RS}(q^{-1})u_{MR}(k) + K_{RR}(q^{-1})y(k)],$$

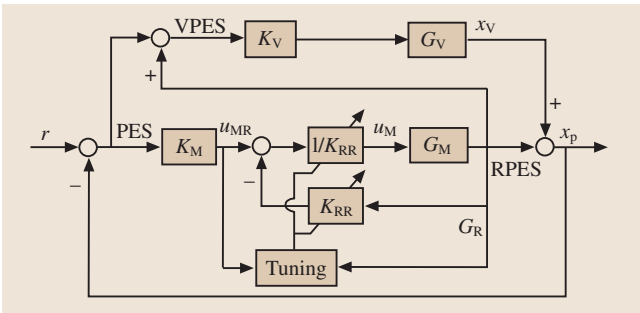


Fig. 32.27 Self-tuning control of the microactuator

where  $u_{MR}$  is the control input to the microactuator;  $y$  denotes the position of the microactuator relative to the VCM, i.e.  $y = RPES$ . Defining:

$$S(q^{-1}) = b_0 K_{RS}(q^{-1}) = s_0 + s_1 q^{-1}, \quad (32.25)$$

$$R(q^{-1}) = b_0 K_{RR}(q^{-1}) = r_0 + r_1 q^{-1}, \quad (32.26)$$

the regressor vector,  $\phi(k)$  and filtered regressor vector,  $\phi_f(k)$ ,

$$\phi(k) = [u_{MR}(k) \ u_{MR}(k-1) \ y(k) \ y(k-1)], \quad (32.27)$$

$$A_c(q^{-1}) \phi_f(k) = (1 + z_o q^{-1}) \phi(k), \quad (32.28)$$

and the controller parameter vector  $\theta = [s_0 \ s_1 \ r_0 \ r_1]^T$ , the closed loop  $RPES$  dynamics (32.25) can be rewritten as

$$y(k) = \theta^T \phi_f(k-1). \quad (32.29)$$

From (32.29), the controller parameter vector estimate  $\hat{\theta}(k) = [\hat{s}_0(k) \ \hat{s}_1(k) \ \hat{r}_0(k) \ \hat{r}_1(k)]^T$  can be updated using a standard recursive least square algorithm (RLS) [32.41]:

$$\hat{\theta}(k) = \hat{\theta}(k-1) + P(k) \phi_f(k) e^o(k), \quad (32.30)$$

$$e^o(k) = y(k) - \hat{\theta}^T(k-1) \phi_f(k-1), \quad (32.31)$$

$$P(k) = \left[ \begin{array}{c} P(k-1) - \\ \frac{P(k-1) \phi_f(k-1) \phi_f^T(k-1) P(k-1)}{1 + \phi_f^T(k-1) P(k-1) \phi_f(k-1)} \end{array} \right], \quad (32.32)$$

The control law is

$$\begin{aligned} \hat{S}(k, q^{-1}) u_{MR}(k) \\ = \hat{S}_o(k) u_M(k) - \hat{R}(k, q^{-1}) y(k), \end{aligned} \quad (32.33)$$

with

$$\hat{S}(k, q^{-1}) = \hat{s}_0(k) + \hat{s}_1(k) q^{-1}, \quad (32.34)$$

$$\hat{R}(k, q^{-1}) = \hat{r}_0(k) + \hat{r}_1(k) q^{-1}, \quad (32.35)$$

and  $u_{MR}(k)$  being the output of the microactuator fixed outer loop compensator  $K_M$ ,  $u_M(k)$  being the control input to the microactuator.

### Dual-Stage Track-Following Control Design Using $\mu$ -Synthesis

$\mu$ , the structured singular value, is a measure of how big a perturbation to a system needs to be to make the system unstable. By incorporating a fictitious uncertainty block, robust performance in terms of  $H_\infty$  norm of the closed loop transfer function can be related to the value of  $\mu$ .  $\mu$ -synthesis is a robust optimal controller design technique that attempts to minimize  $\mu$  through an iterative process [32.43].

**Design Methodology.** For controller design using  $\mu$ -synthesis, the model uncertainties are represented using linear fractional transformations (LFT). Disturbances and outputs are weighted to characterize the real plant environment and the performance requirements. A block diagram used for dual-stage  $\mu$ -synthesis controller design is shown in Fig. 32.28.

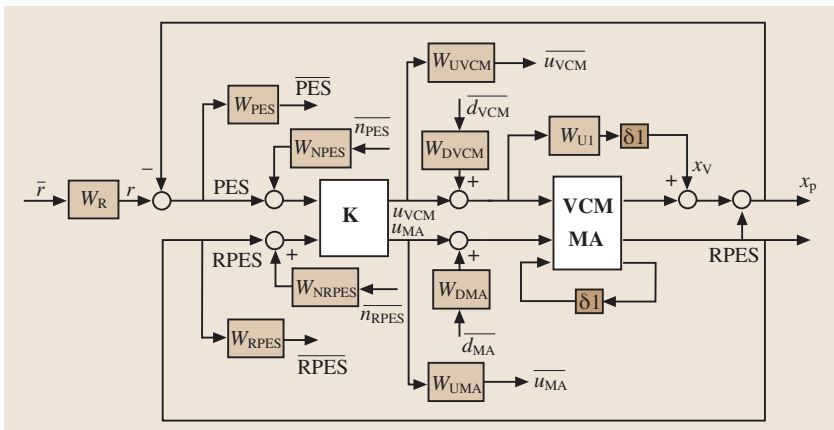


**Fig. 32.28**  $\mu$ -synthesis design block diagram

In the block diagram, two model uncertainties,  $\delta_1$  and  $\delta_2$ , are considered.  $\delta_1$  is an additive uncertainty used to describe the VCM unmodeled dynamics.  $\delta_2$  represents the parametric uncertainty in the stiffness of the microactuator.

Disturbance signals accounted for in the model include the track runout  $r$ , input disturbances to the VCM, and microactuator,  $d_{VCM}$  and  $d_{MA}$ , respectively, the  $PES$  sensor noise  $n_{PES}$  and the  $RPES$  sensor noise  $n_{RPES}$ . These disturbance signals are generated by passing normalized signals  $\bar{r}$ ,  $\overline{d_{VCM}}$ ,  $\overline{d_{MA}}$ ,  $\overline{n_{PES}}$ , and  $\overline{n_{RPES}}$  through weighting functions  $W_r$ ,  $W_{dVCM}$ ,  $W_{dMA}$ ,  $W_{nPES}$ , and  $W_{nRPES}$ , respectively, which can be either constants or frequency shaping filters. These weights are selected by the designer so that disturbances are modeled with sufficient fidelity.

The output signals in the synthesis model are head position error signal,  $PES$ , the microactuator relative position signal,  $RPES$ , the VCM control input  $u_{VCM}$ , and the microactuator control input  $u_{MA}$ . These signals are multiplied by scaling factors,  $W_{PES}$ ,  $W_{RPES}$ ,  $W_{uVCM}$ , and  $W_{uMA}$ , respectively, to produce the weighted performance signals  $\overline{PES}$ ,  $\overline{RPES}$ ,  $\overline{u_{VCM}}$ ,  $\overline{u_{MA}}$ . The scaling factors are selected to characterize the performance requirements.

Given a set of input and output weights and plant uncertainties, if the synthesized controller achieves

$$\mu \leq \beta, \quad (32.36)$$

the closed loop transfer function,  $\overline{T}$ , from the normalized disturbances

$$\overline{d} = [\overline{r} \ \overline{d_{VCM}} \ \overline{d_{MA}} \ \overline{n_{PES}} \ \overline{n_{RPES}}], \quad (32.37)$$

to the weighted performance signals

$$\overline{e} = [\overline{PES} \ \overline{RPES} \ \overline{u_{VCM}} \ \overline{u_{MA}}], \quad (32.38)$$

will have infinity norm

$$\|\overline{T}\|_{\infty} \leq \beta, \quad (32.39)$$

for perturbations

$$\|\Delta\|_{\infty} = \left\| \begin{bmatrix} \delta_1 & 0 \\ 0 & \delta_2 \end{bmatrix} \right\|_{\infty} \leq \frac{1}{\beta}. \quad (32.40)$$

The interpretation of  $H_{\infty}$  as the RMS gain of the sinusoid to help understand the design is as follows. Assume that each element  $\overline{d}_i$  of the disturbance input

vector in (32.37) is a sinusoid of the form

$$\overline{d}_i(t) = D_i \sin(\omega_i t + \psi_i), \quad (32.41)$$

such that

$$\sum_{i=1}^5 D_i^2 \leq 1. \quad (32.42)$$

Then the steady state response of output in (32.38) will also be a sinusoid of the form

$$\overline{e}_i(t) = E_i \sin(\omega_i t + \phi_i), \quad (32.43)$$

and

$$\sum_{i=1}^4 E_i^2 \leq \beta, \quad (32.44)$$

under the perturbations in (32.40).

**Weighting Functions for  $\mu$ -Synthesis Design.** Performance weights are chosen based on limits that the error signals should not exceed. The limit on the  $PES$  is based on a rule of thumb commonly used in the disk drive industry which states that the position error of the head should not exceed 1/10 of a track width during track following.  $RPES$  is limited by the stroke limit of the microactuator. Thus,

$$W_{PES} = \frac{10}{\text{track width}}; \quad W_{RPES} = \frac{1}{\text{stroke limit}}. \quad (32.45)$$

Weights on control inputs are based on the control input saturations.

$$W_{uVCM} = \frac{1}{(iV)_{\max}}; \quad W_{uMA} = \frac{1}{(vM)_{\max}}, \quad (32.46)$$

where  $(iV)_{\max}$  and  $(vM)_{\max}$  are the maximum drive current of the VCM and the maximum drive voltage of the microactuator, respectively.

The weights for  $PES$  noise,  $n_{PES}$ , and the disturbance to the VCM,  $w_{dVCM}$ , were determined by extrapolating the  $PES$  decomposition results presented in [32.29]. The weight of the  $RPES$  sensing noise,  $n_{RPES}$ , is assumed to be 8 nm [32.14]. The disturbance weight,  $w_{dMA}$ , is assumed to be 0.1 V in the design.

The runout weighting is a low pass filter that captures the combined effects of track runout, mechanical vibrations, and bias force disturbance to  $PES$ ,

$$W_r = \frac{2 * 10^{-8} (s + 2\pi * 10)^2}{(s + 2\pi * 1000)^2}. \quad (32.47)$$

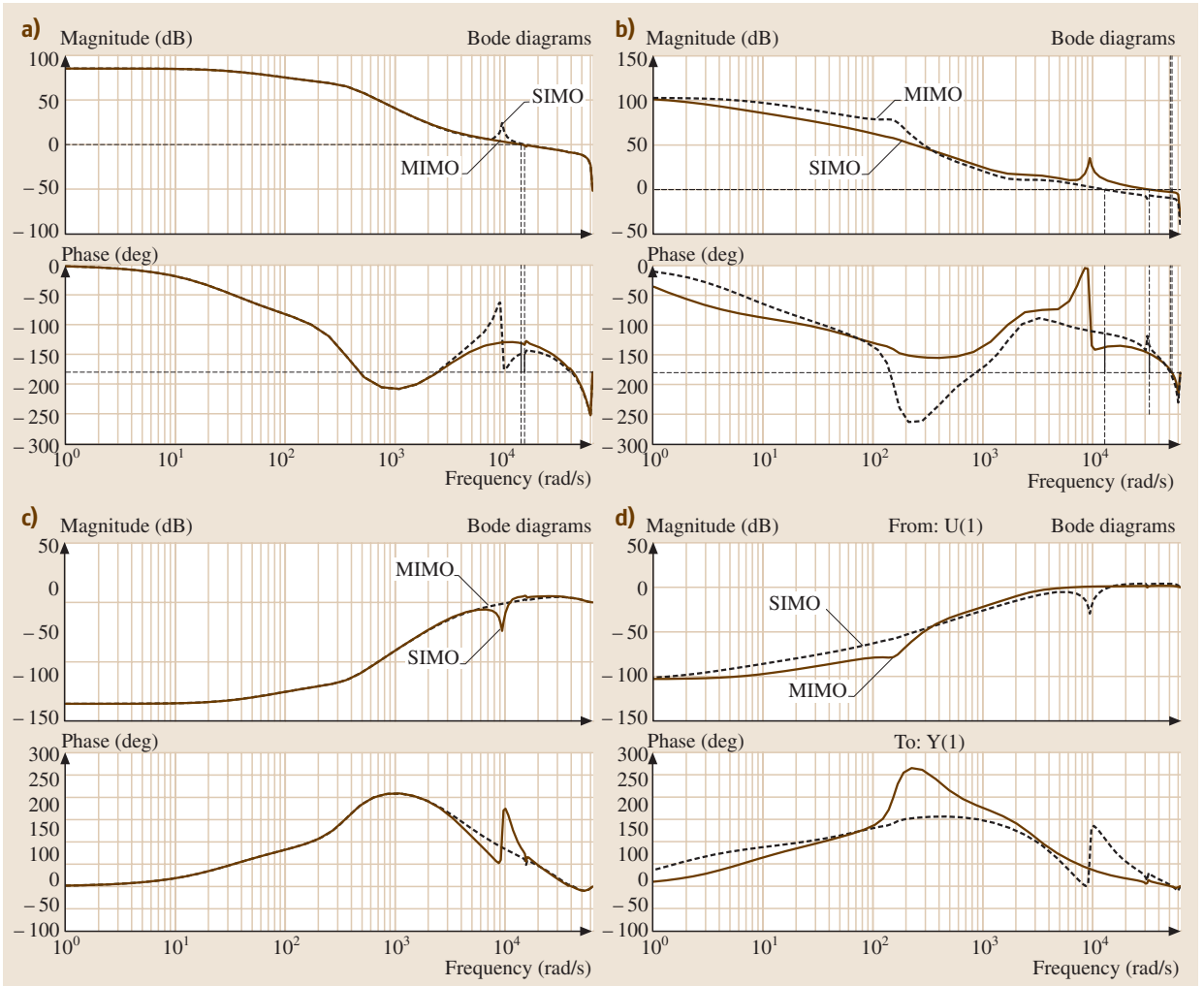


**Fig. 32.29** (a) Open loop Bode plot of the decoupled design; (b) open loop Bode plot of the μ-synthesis design; (c) closed loop sensitivity Bode plot of the decoupled design; (d) closed loop sensitivity Bode plot of the μ-synthesis design

The combination of  $W_{PES}$  and  $W_r$  determines the closed loop sensitivity function from  $r$  to  $PES$ ,  $S(s)$ , of the dual-stage system.

$$\|W_{PES}S(s)W_r\|_{\infty} \leq \beta. \tag{32.48}$$

If  $\beta = 1$ , the magnitude of bode plot of  $S(s)$  lies below that of  $1/W_{PES}W_r$ .

For SIMO design, the controller to be synthesized has only one input. In the synthesis model,  $RPES$  is not fed to the controller  $K$ , and  $RPES$  noise  $n_{rpes}$  and its weights  $W_{nRPES}$  are not used.

### Design and Simulation Results

Figure 32.29 shows the Bode plots of the open loop transfer functions from  $r$  to  $x_p p$  and the closed loop sensitivity functions of the two designs, respectively. Sampling frequency was chosen to be 20 kHz in both designs.

For the decoupled MIMO design, the gain crossover frequency, gain margin, phase margin of the open loop system are 2,201 Hz, 9.1 dB, and 48.8°, respectively. For

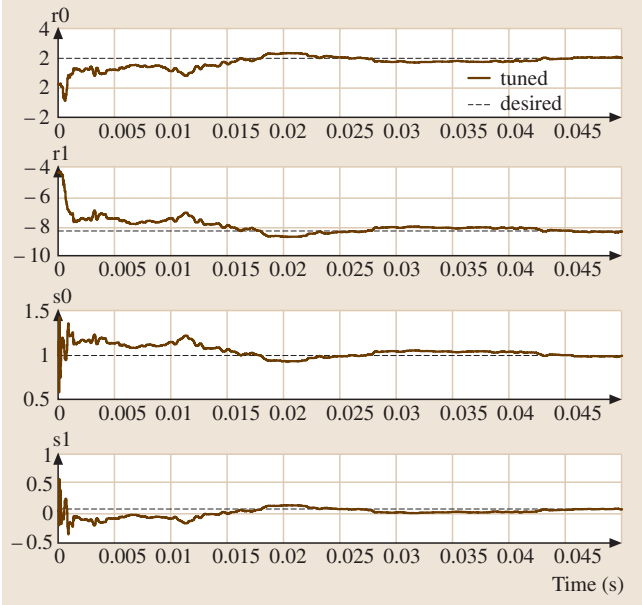


Fig. 32.30 Control parameters adaptation response

the decoupled SIMO design, they are 2,381 Hz, 8.7 dB, and 30.6°, respectively.

For  $\mu$ -synthesis MIMO design, the gain crossover frequency, gain margin, phase margin of the open loop system are 2,050 Hz, 9.5 dB, 66.0°, respectively. For  $\mu$ -synthesis SIMO design, they are 2,223 Hz, 2.9 dB, 32.0°, respectively.

The above controller designs have not been implemented on a MEMS microactuator dual-stage servo system. Controllers designed using both methods have been tested on a PZT actuated suspension dual-stage servo system, however, validating their effectiveness [32.44].

Figure 32.30 shows the simulation of control parameters adaptation for the self-tuning controller, when the real microactuator resonance frequency is 1.2 times its nominal value. The controller parameters converged to their desired values. Similar responses were obtained when the real resonance frequency is 0.8 times the nominal value.

### 32.3.4 Dual-Stage Seek Control Design

Because the inertia of a microactuator is much smaller than that of the VCM, it can produce a larger acceleration and move faster than the VCM. The motion range of a microactuator is usually limited to

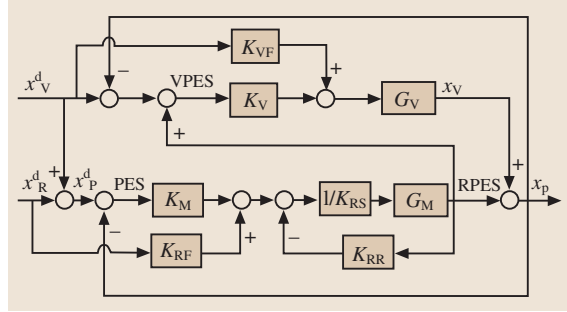


Fig. 32.31 Dual-stage seek control design

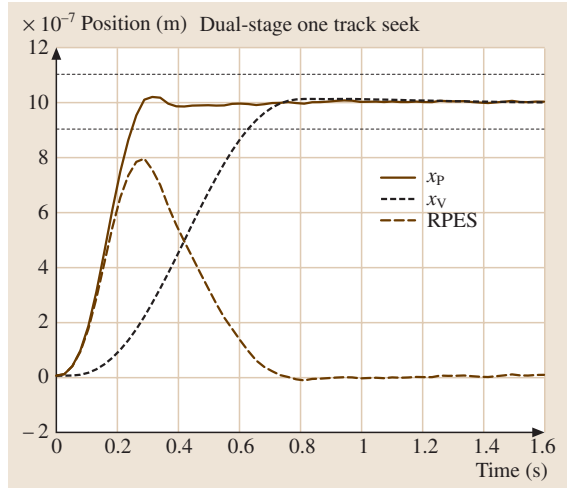


Fig. 32.32 Dual-stage short span seek response

a few micrometers, however. Thus the performance improvement in seek control made possible by using

dual-stage actuation will mainly be in short distance seeks.

Two degree-of-freedom (DOF) position control has been a very popular control technique in short distance seeks. A 2-DOF control technique utilizing decoupled feed forward reference trajectories has been developed for short span seek control using a PZT actuated suspension dual-stage servo system [32.45]. The same technique can also be applied to seek control of MEMS microactuator dual-stage servo system.

Figure 32.31 shows a block diagram for dual-stage short span seek control design using this method. In the figure,  $x_V^d$  and  $x_R^d$  are the desired seek trajectories of the VCM and the microactuator respectively.  $K_{VF}$  and  $K_{RF}$  are Zero Phase Error Tracking Feed Forward Controllers (ZPETFFC) generated with the VCM model  $G_V$  and the damped microactuator model  $G_R$  [32.46].

To minimize the residual vibration after seek operation, minimum jerk seek trajectories were applied to both the VCM and the microactuator. These can be generated

by [32.47]

$$x_V^d(t) = 60 d_s \left[ \frac{1}{10} \left( \frac{t}{T_V} \right)^5 - \frac{1}{4} \left( \frac{t}{T_V} \right)^4 + \frac{1}{6} \left( \frac{t}{T_V} \right)^3 \right], \tag{32.49}$$

$$x_R^d = \begin{cases} 60 (d_s - x_V^d(T)) \\ \times \left[ \frac{1}{10} \left( \frac{t}{T} \right)^5 - \frac{1}{4} \left( \frac{t}{T} \right)^4 + \frac{1}{6} \left( \frac{t}{T} \right)^3 \right] & t \leq T, \\ d_s - x_V^d(t) & t > T \end{cases} \tag{32.50}$$

where  $d_s$  is the distance of the head from the target track;  $T$  is the time when the head reaches the target track if dual-stage actuator is used, while  $T_V$  is the time when the head reaches the target track if only VCM is used.  $T_V$  and  $T$  can be chosen based on the control force saturation and seek performance requirements.

Figure 32.32 shows the 1  $\mu$ m seek responses of the dual-stage actuator for the MIMO design. Overshoot was eliminated, and no obvious residual vibrations occurred. The seek time using the dual-stage actuator is about 0.25 ms, compared to a seek time of about 0.7 ms if only the VCM is used.

## 32.4 Conclusions and Outlook

In order to increase hard disk drive storage density, high bandwidth dual-stage servo systems are necessary to suppress disturbances and increase servo precision. Various prototype MEMS microactuators have been designed and fabricated to provide a dual-stage actuation system. The most common approach for these prototypes is to use electrostatic driving arrays produced by MEMS fabrication methods.

MEMS microactuators provide a potentially high performance and low cost solution for achieving the servo requirements for extremely high HDD storage density. Simulations and experiments show that many MEMS microactuator features, such as integrated silicon gimbals and capacitive relative position sensing arrays, can meet important requirements for operation of HDDs. The use of structural electrical-isolation in the microactuator design could considerably reduce microactuator driving voltages, while processes that avoid the use of silicon-on-insulator wafers or high-temperature processing steps could reduce manufacturing costs. High bandwidth dual-stage track-following controllers have been designed using both a decoupled SISO design

method and robust  $\mu$ -synthesis design method, among others. In addition, short-span seeking control using a 2-DOF control structure with decoupled feed forward trajectory generation can greatly reduce the short span seek time.

But research remains to be done in the areas of system integration, reliability, and performance enhancement for this technology to be utilized in commercial products. Cost and reliability are probably the most important obstacles to commercial implementation of actuated slider dual-stage servo systems at this time. Streamlining of microactuator fabrication processes or development of a process compatible with that of the slider and head fabrication could reduce manufacturing costs, which are not quite yet economical. Meanwhile, dynamic behavior and reliability of the microactuator under disturbances from airflow, head-disk interaction, and particle presence are being experimentally studied by industry.

Further in the future, to achieve nanometer servo precision, third-generation dual-stage servo systems will have to employ an actuated head approach. Research in

this area has just started, with the key problem being how to combine microactuator fabrication with read/write head fabrication. Another area of research is the use of MEMS technology to incorporate additional sensors, such as accelerometers and strain gauge vibration sensors, to suppress the TMR due to airflow and external disturbances excited structural vibrations. New robust, adaptive MIMO control architectures and algorithms must be developed for such a multisensing and multiactuation servo system.

Besides the application of MEMS microactuators in dual-stage servo control of traditional rotating media magnetic HDDs, recent advances in MEMS and nanotechnology have made possible the development of a new class of miniaturized ultra-high density storage devices that use probe arrays for recording and reading data. This new architecture abandons the traditional

rotating media and flying slider paradigm in favor of parallel  $x$ - $y$  scanning of entire probe arrays over a storage medium. The probe arrays and/or the media are moved with electrostatic or electromagnetic microactuators that generate  $x$ - $y$  in-plane relative motion, as well as  $z$ -axis out-of-plane relative motion. One example of this new generation of storage devices is IBM's "millipede," which utilizes atomic force microscopy (AFM) recording technology [32.48]. Data is recorded on a polymer media by tiny depressions melted by a thermomechanical process by the AFM tips. 400 Gb/in.<sup>2</sup> bit patterns have been demonstrated using thermal probes.

By any of the paths above, MEMS and nanotechnology will become a basic enabling technology for the development of future data storage devices, offering the capabilities of small size, low power consumption, ultra-high densities, low cost, and high performance.

## References

- 32.1 T. Yamaguchi: Modelling and control of a disk file head-positioning system, Proc. Inst. Mech. Eng. I (J. Syst. Cont. Eng.) **215** (2001) 549–567
- 32.2 T. Howell, R. Ehrlick, M. Lippman: TPI growth is key to delaying superparamagnetism's arrival, Data Stor. (1999) 21–30<sup>TS5</sup>
- 32.3 R. B. Evans, J. S. Griesbach, W. C. Messner: Piezoelectric microactuator for dual-stage control, IEEE Trans. Magn. **35** (1999) 977–81
- 32.4 I. Naniwa, S. Nakamura, S. Saegusa, K. Sato: Low voltage driven piggy-back actuator of hard disk drives, IEEE International MEMS 99 Conference, Orlando 1999 (, 49–52<sup>TS10</sup>)
- 32.5 D. Horsley: Microfabricated electrostatic actuators for magnetic disk drives. PhD Thesis (University of California, Berkeley 1998)
- 32.6 L. Muller: Gimballed electrostatic microactuators with embedded interconnects. PhD Thesis (University of California, Berkeley 2000)
- 32.7 S. Koganezawa, K. Takaishi, Y. Mizoshita, Y. Uematsu, T. Yamada: Development of integrated piggyback milli-actuator for high density magnetic recording, International Conference on Micromechatronics for Information and Precision Equipment 1997 (, 20–23<sup>TS6</sup>)
- 32.8 L.-S. Fan, T. Hirano, J. Hong, P. R. Webb, W. H. Juan, W. Y. Lee, S. Chan, T. Semba, W. Imano, T. S. Pan, S. Pattanaik, F. C. Lee, I. McFadyen, S. Arya, R. Wood: Electrostatic microactuator and design considerations for hdd application, IEEE Trans. Magn. **35** (1999) 1000–5
- 32.9 T. Imamura, M. Katayama, Y. Ikegawa, T. Ohwe, R. Koishi, T. Koshikawa: MEMS-based integrated head/actuator/slider for hard disk drives, IEEE/ASME Trans. Mechatron. **3** (1998) 166–74
- 32.10 T. Imamura, T. Koshikawa, M. Katayama: Transverse mode electrostatic microactuator for MEM-based HDD slider, Proc. IEEE MEMS Workshop, San Diego 1996 (IEEE, 216–21<sup>TS7</sup>)
- 32.11 S. Nakamura, K. Suzuki, M. Ataka, H. Fujita: An electrostatic micro actuator for a magnetic head tracking system of hard disk drives, Transducers '97, Chicago 1999 (, 1081–84<sup>TS10</sup>)
- 32.12 Y. Soeno, S. Ichikawa, T. Tsuna, Y. Sato, I. Sato: Piezoelectric piggy-back microactuator for hard disk drive, IEEE Trans. Magn. **35** (1999) 983–87<sup>TS8</sup>
- 32.13 Y. Li, R. Horowitz: Mechatronics of electrostatic microactuator for computer disk drive dual-stage servo systems, IEEE/ASME Trans. Mechatron. **6** (2001) 111–21
- 32.14 N. Wongkomet: Position sensing for electrostatic micropositioners. PhD Thesis (University of California, Berkeley 1998)
- 32.15 A. Hac, L. Liu: Sensor and actuator location in motion control of flexible structures, J. Sound Vib. **167** (1993) 239–61
- 32.16 K. Hiramoto, H. Doki, G. Obinata: Optimal sensor/actuator placement for active vibration control using explicit solution of algebraic Riccati equation, J. Sound Vib. **229** (2000) 1057–75
- 32.17 P. Cheung, R. Horowitz, R. Howe: Design, fabrication and control of an electrostatically driven

<sup>TS5</sup> Please provide volume number.

<sup>TS6</sup> Please provide place of proceeding, editors, publisher, place and year of publication.

<sup>TS7</sup> Please provide place of proceeding, editors, and place and year of publication.

<sup>TS8</sup> Should "microactuator" be "microactuator"?

- polysilicon microactuator, IEEE Trans. Magn. **32** (1996) 122–128
- 32.18 T. Chen, Y. Li, K. Oldham, R. Horowitz: MEMS application in computer disk drive dual-stage servo systems, J. Soc. Instrum. Control Eng. **41** (2002) 412–20
- 32.19 T.-L. Chen: Design and fabrication of PZT-actuated silicon suspensions for hard disk drives. PhD Thesis (University of California, Berkeley 2001)
- 32.20 C. G. Keller, R. T. Howe: HexSil tweezers for tele-operated micro-assembly, 10th Int'l Workshop on Micro Electro Mechanical Systems TS<sup>9</sup> (MEMS'97), Nagoya 1997 (, 72–77 TS<sup>10</sup>)
- 32.21 T. J. Brosnihan, J. M. Bustillo, A. P. Pisano, R. T. Howe: Embedded interconnect and electrical isolation for high-aspect-ratio, SOI inertial instruments, International Conference on Solid-State Sensors and Actuators, New York 1997 (, 637–40 TS<sup>10</sup>)
- 32.22 T. Hirano, L.-S. Fan, T. Semba, W. Y. Lee, J. Hong, S. Pattanaik, P. Webb, W.-H. Juan, S. Chan: Micro-actuator for tera-storage, IEEE Int'l MEMS 1999 Conference, Orlando 1999 (IEEE, 6441–6 TS<sup>7</sup>)
- 32.23 T. Hirano, L.-S. Fan, T. Semba, W. Lee, J. Hong, S. Pattanaik, P. Webb, W.-H. Juan, S. Chan: High-bandwidth HDD tracking servo by a moving-slider micro-actuator, IEEE Trans. Magn. **35** (1999) 3670–72
- 32.24 T. Iizuka, T. Oba, H. Fugita: Electrostatic micro actuators with high-aspect-ratio driving gap for hard disk drive applications, Int'l Symposium on micro-mechatronics and human science, Nagoya 2000 (, 229–36 TS<sup>10</sup>)
- 32.25 H. Kuwajima, K. Matsuoka: Thin film piezoelectric dual-stage actuator for HDD, InterMag Europe, Session BS04, Amsterdam 2002 (, BS4 TS<sup>10</sup>)
- 32.26 Y. Lou, P. Gao, B. Qin, G. Guo, E.-H. Ong, A. Takada, K. Okada: Dual-stage servo with on-slider PZT microactuator for hard disk drives, InterMag Europe, Session BS03, Amsterdam 2002 (, TS<sup>11</sup>)
- 32.27 H. Fujita, K. Suzuki, M. Ataka, S. Nakamura: A microactuator for head positioning system of hard disk drives, IEEE Trans. Magn. **35** (1999) 1006–10
- 32.28 B.-H. Kim, K. Chun: Fabrication of an electrostatic track-following micro actuator for hard disk drives using SOI wafer, J. Micromech. Microeng. **11** (2001) 1–6
- 32.29 R. Ehrlich, D. Curran: Major HDD TMR sources, and projected scaling with TPI, IEEE Trans. Magn. **35** (1999) 885–91
- 32.30 K. Mori, T. Munemoto, H. Otsuki, Y. Yamaguchi, K. Akagi: A dual-stage magnetic disk drive actuator using a piezoelectric device for a high track density, IEEE Trans. Magn. **27** (1991) 5298–300
- 32.31 S. J. Schroeck, W. C. Messner, R. J. McNab: On compensator design for linear time-invariant dual-input single-output systems, IEEE/ASME Trans. Mechatron. **6** (2001) 50–57
- 32.32 T. Semba, T. Hirano, L.-S. Fan: Dual-stage servo controller for HDD using MEMS actuator, IEEE Trans. Magn. **35** (1999) 2271–73
- 32.33 T. Suzuki, T. Usui, M. Sasaki, F. Fujisawa, T. Yoshida, H. Hirai: Comparison of robust track-following control systems for a dual stage hard disk drive, Proc. of International Conference on Micromechatronics for Information and Precision Equipment, Tokyo 1997 (, 101–18 TS<sup>10</sup>)
- 32.34 X. Hu, W. Guo, T. Huang, B. M. Chen: Discrete time LQG/LTR dual-stage controller design and implementation for high track density HDDs, Proc. of American Automatic Control Conference, San Diego 1999 (, 4111–15 TS<sup>10</sup>)
- 32.35 S.-M. Suh, C. C. Chung, S.-H. Lee: Design and analysis of dual-stage servo system for high track density HDDs, Microsyst. Technol. **8** (2002) 161–68
- 32.36 D. Hernandez, S.-S. Park, R. Horowitz, A. K. Packard: Dual-stage track-following servo design for hard disk drives, Proc. of American Automatic Control Conference, San Diego 1999 (, 4116–21 TS<sup>10</sup>)
- 32.37 M. Rotunno, R. A. de Callafon: Fixed order  $H_\infty$  control design for dual-stage hard disk drives, Proc. of the 39th IEEE Conference on Decision and Control, Sydney 2000 (, 3118–19 TS<sup>10</sup>)
- 32.38 S.-H. Lee, S.-E. Baek, Y.-H. Kim: Design of a dual-stage actuator control system with discrete-time sliding mode for hard disk drives, Proc. of the 39th IEEE Conference on Decision and Control, Sydney 2000 (, 3120–25 TS<sup>10</sup>)
- 32.39 M. Sasaki, T. Suzuki, E. Ida, F. Fujisawa, M. Kobayashi, H. Hirai: Track-following control of a dual-stage hard disk drive using a neuro-control system, Eng. Appl. Artif. Intell. **11** (1998) 707–16
- 32.40 D. Horsley, N. Wongkomet, R. Horowitz, A. Pisano: Precision positioning using a microfabricated electrostatic actuator, IEEE Trans. Magn. **35** (1999) 993–99
- 32.41 K. J. Åström, B. Wittenmark: *Adaptive Control*, 2 edn. (Addison-Wesley, 1995) TS<sup>12</sup>
- 32.42 M. T. Whilte, W.-M. Lu: Hard disk drive bandwidth limitations due to sampling frequency and computational delay, Proc. of the 1999 IEEE/ASME International Conference on Intelligent Mechatronics, Atlanta 1999 (, 120–25 TS<sup>10</sup>)
- 32.43 G. J. Balas, J. C. Doyle, K. Glover, A. Packard, R. Smith:  *$\mu$ -Analysis and Synthesis Toolbox* (MUSYN Inc. and The MathWorks, 1995) TS<sup>13</sup>
- 32.44 Y. Li, R. Horowitz: Design and testing of track-following controllers for dual-stage servo systems with PZT actuated suspensions [in HDD], Microsyst. Technol. **8** (2002) 194–205

TS<sup>9</sup> Is this the correct spelling?

TS<sup>10</sup> Please provide editors, publisher, place and year of publication.

TS<sup>11</sup> Please provide editors, publisher, place and year of publication, and page numbers.

TS<sup>12</sup> Please provide publishers location.

TS<sup>13</sup> Please provide location of publication.

- 32.45 M. Kobayashi, R. Horowitz: Track seek control for hard disk dual-stage servo systems, *IEEE Trans. Magn.* **37** (2001) 949–54
- 32.46 M. Tomizuka: Zero phase error tracking algorithm for digital control, *Trans. ASME, J. Dynam. Syst. Meas. Control* **109** (1987) 65–68
- 32.47 Y. Mizoshita, S. Hasegawa, K. Takaishi: Vibration minimized access control for disk drive, *IEEE Trans. Magn.* **32** (1996) 1793–98
- 32.48 P. Vettiger, G. Cross, M. Despont, U. Drechsler, U. Durig, B. Gotsmann, W. Haberle, M.A. Lantz, H.W. Rothuizen, R. Stutz, G.K. Binnig: The “millipede” – nanotechnology entering data storage, *IEEE Trans. Nanotechnol.* **1** (2002) 39–55